약학박사학위논문

인간 threonyl-tRNA synthetase의 혈관신생인자 및 뮤신 생합성 조절 기전에 관한 연구

Studies of the regulatory mechanisms of human threonyl-tRNA synthetase in the biosynthesis of angiogenic factors and mucin

2017년 8월

서울대학교 대학원
약학과 의약생명과학전공
정 승 재

Abstract

Aminoacyl-tRNA synthetases (ARSs) are essential enzymes for protein synthesis to link specific amino acids to their cognate tRNAs. Recent studies have shown that ARSs, considered as a sort of "housekeeping" enzyme, are now involved in a variety of functions such as transcription, translation, proliferation, inflammation, angiogenesis and cell death. This study is focused on the human threonyl-tRNA synthetase (TRS) and its potential role.

In chapter I, the results show that human TRS functions as a translational initiation factor to regulate vertebrate-specific translation initiation via eIF4E homologous protein (4EHP). TRS selectively interacts with 4EHP in a manner similar to the eIF4G interaction with eIF4E. In this way, TRS acts as a scaffold protein to assemble eIF4A, consequently forming eIF4F-like complex. Importantly, complex formation is evolutionary gain-of-function to control protein synthesis of a subset of mRNAs necessary for development of the vertebrate system, verified by endothelial cell migration and vessel formation as well as in vivo zebrafish embryo vascularization assays.

In chapter II, the results show that TRS specifically regulates biosynthesis of mucin1 (MUC1) through catalytic activity. The levels of MUC1 protein are affected by threonine and biosynthesis of MUC1 in pancreatic cancer is sensitive to the activity and expression of TRS that incorporates threonine to MUC1. TRS catalytic inhibitors and threonine starvation attenuate MUC1-dependent pancreatic cancer cell migration. In addition, tissue levels of TRS and MUC1 are positively correlated in clinical tumor specimen and expression of both proteins at high level is associated with poor survival outcome of the patients.

To summarize, chapter I study discovers an unexpected role of TRS in regulating translation initiation in vertebrates and uncovers a previously unidentified cap-dependent translation initiation mechanism that represents an evolutionary gain of function in vertebrates. Chapter II study provides several evidences showing the potential role of TRS in the migration of human pancreatic cancer cells by enhancing MUC1 biosynthesis, suggesting a novel insight into targeting TRS as a new way to pancreatic cancer.

Keywords: Threonyl-tRNA synthetase, eIF4E homologous protein, Crystal structure, Translation initiation, Mucin 1, Pancreatic cancer, Cell migration

Student number: 2008-21809

Contents

Chapter I.

Threonyl-tRNA synthetase activates vertebrate-specific translational initiation via eIF4E homologous protein

Chapter II.
Inhibition of MUC1 biosynthesis via threonyl-tRNA synthetase suppresses pancreatic cancer cell migration

List of figures and tables

Chapter I.
Threonyl-tRNA synthetase activates vertebrate-specific translational initiation via eIF4E homologous protein

Chapter II.
Inhibition of MUC1 biosynthesis via threonyl-tRNA synthetase suppresses pancreatic cancer cell migration

Chapter I.

Threonyl-tRNA synthetase activates vertebrate-specific translational initiation via eIF4E homologous protein

Running title: Translational initiation control via the interaction with 4EHP

Keywords: Threonyl-tRNA synthetase, translation initiation, eIF4E homologous protein, crystal structure, protein-protein interaction

1

Abbreviation

TRS : Threonyl-tRNA synthetase

4EHP : eIF4E homologous protein

eIF4E : eukaryotic translation initiation factor 4E

eIF4G : eukaryotic translation initiation factor 4G

eIF4A : eukaryotic translation initiation factor 4A

eIF4F : eukaryotic translation initiation factor 4F

4E-BP1 : eIF4E-binding protein 1

5'UTR : 5' untranslated region

ARS : Aminoacyl-tRNA synthetase

UNE-T : Unique N-terminal region

V-eIF4F : Vertebrate-specific eIF4F-like complex

PABP : Poly(A)-binding protein

RIP-seq : RNA-immunoprecipitation deep sequencing

GO : Gene ontology

VEGF : Vascular endothelial growth factor

Abstract

While control of general translation initiation via the eIF4E-mediated complex has been intensively studied, little is known about how its homologous protein, 4E-HP controls translation, in vertebrates. Herein, study reports a novel and unique translation initiation complex consisting of threonyl-tRNA synthetase (TRS) and eIF4E homologous protein (4EHP) as a gain of function event in the vertebrate lineage. While the complex of 4EHP and the unique N-terminal region of TRS showed structural homology with previously known translation initiation complexes of eIF4E-eIF4G and eIF4E-4E-BP1, it plays a distinct role in the translational initiation of a specific mRNA group required for vertebrate development such as vascularization. In addition to 4EHP, TRS recruited eIF4A and poly(A)-binding protein for linking the complex to the 40S ribosome. For the selection of target mRNAs, TRS recognizes a tRNA^{Thr} anticodon loop-mimicking structure in the 5' untranslated region of specific mRNAs. The functional significance of the TRS-4EHP complex was validated by examining its role in endothelial tube formation and in vivo zebrafish vascularization models. The results show that TRS plays a dual role in vertebrate-specific translational initiation, first as a scaffold to assemble other initiation components and second as a selector of target mRNAs.

Introduction

Protein synthesis is one of the most fundamental biological processes, and it is mainly regulated at the initiation step (1). The predominant cap-dependent translation initiation, that principally controls cellular abundance of proteins (1-3), is a multistep process involving a series of reactions that eventually culminate in the recruitment of 80S ribosome to mRNA (4). This initiation process begins with the recognition of the 7-methylguanosine (m^7GpppN) 5′-cap of mRNAs by eukaryotic translation initiation factor (eIF) 4F (eIF4F), the main mRNA-binding component of the translation machinery (5). Thus, the association of eIF4F with a 5′-cap structure is the most critical aspect of translation initiation. eIF4F consists of three subunits: eIF4E, the cap-binding protein central to global protein synthesis; eIF4A, an RNA helicase that unwinds the secondary structure in 5′ untranslated region (5′ UTR) of mRNAs, thereby permitting small ribosomal subunit to scan along mRNAs and to reach the start codon; and eIF4G, which serves as a scaffolding protein for the assembly of eIF4E and eIF4A. eIF4G also plays a key role in linking mRNAs to ribosome by interacting with ribosome-associated initiation factor eIF3.

 Cap-mediated protein synthesis via eIF4F is not sufficient to meet the demands for life, and additional complexity is required to enable cells to achieve robust, yet specific protein synthesis in different conditions. Best known among alternative mechanisms is internal ribosome entry site-driven translation, which occurs when eIF4F is inactivated in unfavorable stress conditions (6). Besides, selective cap-dependent protein synthesis under hypoxia condition has been proposed that follows inactivation of the global translation initiation

factor eIF4E by mTOR-dependent sequestering (7-10). Oxygen tension was reported to switch principal translation initiation machinery (11). This study identified a hypoxia-stimulated heterotrimeric complex, consisting of oxygen-regulated hypoxia-inducible factor 2a (HIF-2a), RNA-binding protein RBM4, and cap-binding eIF4E homologous protein (4EHP), that regulates global hypoxic protein synthesis. The HIF-2a‐RBM4‐4EHP complex also recruits the RNA helicase eIF4A required for translation initiation.

  While 4EHP binds to the 5′-cap, it does not interact with eIF4G that links mRNAs to ribosome and initiates translation (12, 13). Thus, 4EHP is considered unlikely to stimulate translation initiation, and is instead believed to be a translational repressor. Evidences have been acquired mainly in *Drosophila* (14, 15), and the most profound example is the translational repression of the *caudal* mRNA required for *Drosophila* embryogenesis. *Drosophila* 4EHP directly binds to both the cap of *caudal* mRNA and to Bicoid protein, which tethers to the 3′ UTR of the *caudal* mRNA to repress mRNA translation (14). In mammals, 4EHP forms a complex together with Grb10-interacting GYF protein 2 and the zinc finger protein 598 to repress translation of a subset of mRNAs during embryonic development (16). Thus, these reports suggest unique role of 4EHP in translation initiation, independently of eIF4E. Although the working mechanisms underlying the role of 4EHP in regulating translation initiation as a repressor or an activator in different biological contexts are not well understood, its function may be determined by its binding partners (11, 14-16).

  While aminoacyl-tRNA synthetases (ARSs) are essential enzymes for protein synthesis, these enzymes in higher eukaryotic systems are evolved to adopt unique domains (17) that are not indispensable for

their catalytic reaction. These acquired domains have rendered ARSs the capability of mediating diverse functions via the interactions with various cellular factors (18, 19). This study paid attention to human threonyl-tRNA synthetase (TRS) and its potential role in the control of translational initiation because its prokaryotic counterpart, namely, *Escherichia coli* TRS, represses translation of its own mRNA by binding to 5' UTR region that forms a pseudo-anticodon loop of its cognate tRNA (20). Human TRS shares homology with bacterial counterparts in its catalytic domain and contains unique N-terminal region (UNE-T) (17). These features encouraged to investigate whether human TRS would play a role in translation initiation, and if so, what the function and working mechanism would be.

Here, this report discover that the human TRS functions as a translational initiation factor to regulate vertebrate-specific translation initiation. The results identified that TRS selectively interacts with 4EHP in a manner similar to the eIF4G interaction with eIF4E. In this way, TRS acts as a scaffold protein to assemble eIF4A, consequently forming eIF4F-like complex. Importantly, this study demonstrated that the complex formation is evolutionary gain of function to control protein synthesis of a subset of mRNAs necessary for development of the vertebrate system, verified by endothelial cell migration and vessel formation as well as *in vivo* zebrafish embryo vascularization assays.

Results

Specific interaction of TRS UNE-T region with 4EHP

To have an insight into the function of human TRS beyond its catalysis, cellular factors that could make interactions with this protein were identified using yeast-two hybrid screen and liquid chromatography-mass spectrometry analysis. Both analyses independently revealed a previously unreported interaction of TRS with 4EHP (data not shown) which is known to regulate translation initiation (11, 14-16).

 To validate the specificity of this interaction, HEK293T cells were co-transfected with Strep-TRS and each of FLAG-tagged human eIF4E family proteins including eIF4E1 (generally named as eIF4E), eIF4E2 (4EHP), and eIF4E3. Strep-TRS was pulled down with Strep-Tactin beads and determined co-precipitation of the eIF4E family proteins with anti-FLAG antibody. Among the three eIF4E proteins, eIF4E2 (4EHP), but not eIF4E1 and eIF4E3, was co-precipitated with Strep-TRS (Figure 1A). The interaction between endogenous TRS and 4EHP was confirmed by co-immunoprecipitation in embryonic lung WI-26 cells using anti-TRS antibody (Figure 1B) as well as anti-4EHP antibody (Figure 1C). To determine the specificity toward ARSs, HA-4EHP was expressed with each of human TRS, alanyl-tRNA synthetase (AlaRS) and seryl-tRNA synthetase (SRS) in 293T cells, precipitated with anti-HA antibody, and found the specific co-precipitation of TRS with HA-4EHP (Figure 1D). Next, bimolecular fluorescence complementation (BiFC) assay was conducted to assess the interaction of the two proteins in CHO cells using the N- (VN) and C-terminal (VC) fragments of the Venus fluorescent protein. FLAG-TRS and HA-4EHP or HA-eIF4E

were fused to the N-terminal ends of VN and VC, respectively, and monitored the recovery of green fluorescence. Fluorescence signal was detected only in the cytoplasm of the cells co-transfected with FLAG-TRS-VN and HA-4EHP-VC, but not with FLAG-TRS-VN and HA-eIF4E-VC and with FLAG-AlaRS-VN and HA-4EHP-VC, further supporting the specific interaction of TRS with 4EHP (Figure 1E).

To identify the TRS region responsible for the interaction with 4EHP, different functional domains of TRS were expressed (PDB 1WWT and PDB 1QF6, Figure 1F) and tested for the interaction with 4EHP by co-immunoprecipitation. The results showed the interaction of the N-terminal region of unknown function (UNE-T, residues 180) with 4EHP (Figures 1F and 1G). Isothermal titration calorimetry (ITC) confirmed the interaction between TRS UNE-T and 4EHP, and titration of UNE-T was accompanied by exothermic binding that was fitted to a 1:1 binding model with a K_d of 2.5 M (Figure 1H). Taken together, these results demonstrate the specific interaction of TRS with 4EHP via its UNE-T region.

Structure of the TRS UNE-T and 4EHP complex

To gain functional insight into the TRS and 4EHP interaction, crystallization of the UNE-T (residues 174) and 4EHP complex was conducted using an *in situ* proteolysis technique (21). However, initial attempts were unsuccessful, perhaps because of the dynamic nature of UNE-T. To improve the crystal quality, several truncated variants of UNE-T were tested and finally the crystals of X-ray diffraction quality were obtained from the complex of UNE-T (residues 3074) and 4EHP (residues 45234). The structure was determined by the molecular replacement method using the 4EHP structure (PDB 2JGB)

as a search model and refined to 1.9 Åresolution (Figure 2A and Table S1). The final model included residues Lys45 to Asp219 of 4EHP and Pro49 to Glu74 of TRS UNE-T (Figures 2A and 2B). Residues Pro69Tyr78 and Ser220Val234 of 4EHP, and Gly30Asn48 of TRS, were not included in the final model because they were not observed in the electron density map presumably due to high flexibility. Crystallization of the TRS UNE-T-4EHP complex was carried out in the absence of a m^7GTP cap analog known to bind 4EHP. This might result in the formation of an incomplete binding site for the 7-methylguanine moiety of the cap analog, which is stabilized by a sandwich stacking interaction between Tyr78 located in the flexible region and Trp124 in the previously reported structure (PDB 2JGB) (22). In addition, in the m^7GTP-bound 4EHP structure, the aromatic ring of Trp124 makes van der Waals contacts with Ser220 and Ile221 (22). In this structure, however, the Trp124 side chain adopts a different conformation that may cause residues Ser220Val234 to be disordered and hence invisible in the electron density. Similar structural features were observed in the structure of 4EHP complexed with a 4E-BP1 peptide without m^7GTP (PDB 2JGC) (22). Thus, the overall structure of 4EHP in the complex is similar to the previously determined 4E-BP1 peptide-bound structure (PDB 2JGC) (22), and no substantial conformational changes occur upon TRS UNE-T binding. The structures of TRS or 4E-BP1 bound to 4EHP superimpose with a root-mean-square deviation (RMSD) of 0.25 Å over 133 C atoms (Figure 2C).

The TRS UNE-T region interacting with 4EHP adopts a canonical helix with additional short N- and C-terminal extensions, as previously reported in eIF4G (Figure 2D) and 4E-BP1 (Figure 2E), interacting with eIF4E (23, 24). The complex of TRS UNE-T with

4EHP superimposes well with those of eIF4G or 4E-BP1 with eIF4E (Figure 2F). Recent structural studies demonstrated that eIF4G and 4E-BP1 interact with the dorsal and lateral surfaces of eIF4E via their canonical helix that is connected through an elbow-loop linker and non-canonical loop (Figure 2F) (23, 24). However, neither of elbow-loop linker or non-canonical loop was observed in the TRS UNE-T-4EHP complex (Figure 2F). This may be due to structural features of TRS since the TGS domain (named after TRS, GTPase, and SpoT, PDB 1WWT) (25) following the UNE-T region begins immediately after Asp78 (Figure 2G).

  As a typical class II-type tRNA synthetase (26), human TRS forms a dimer through the catalytic domain. Based on ITC results showing that TRS UNE-T binds to 4EHP with a 1:1 stoichiometry, 4EHP may interact with the UNE-T region of each subunit of the TRS dimer (Figure 2G). Overall, the crystal structure of the TRS UNE-T and 4EHP complex suggests that TRS may play a regulatory role in translation initiation via 4EHP, which may be distinct from the previously reported eIF4E- or 4EHP-mediated regulation of translation initiation.

Structural details of the TRS UNE-T and 4EHP interaction

The TRS UNE-T region engages the dorsal surface of 4EHP through its -helix (Figures 2B). Interactions between the two proteins are mediated by using the canonical eIF4E-binding motif with the consensus sequence YX_4L, where Y, X, L, and indicate Tyr, any amino acid, Leu, and any hydrophobic amino acid, respectively (Figures 3A - 3E) (27, 28). The canonical motif of UNE-T (Figure 3A) is located in a position similar to those in the complexes of 4E-BP1-4EHP (Figure 3B) (22), eIF4G-eIF4E (Figure 3C) (24) and

4E-BP1-eIF4E (Figure 3D) (23). Specifically, the hydroxyl group of Tyr55 in TRS (Tyr612 in eIF4G, and Tyr54 in 4E-BP1) contacts the backbone of His54 and Pro55 in the H54-P55-L56 motif of 4EHP (corresponding to the H37-P38-L39 motif in eIF4E) (Figure 3F). Additionally, Tyr55 makes van der Waals contacts with His54, Leu56, and Val91 in 4EHP, similarly to those observed in the structure of 4E-BP1 complexed with 4EHP (Figure 3F) (22). Similar features to the TRS Tyr55-mediated interactions with 4EHP are also present in the structures of eIF4G and 4E-BP1 complexed with eIF4E (Figure 3F) (23, 24). The residue corresponding to L in the consensus sequence YX_4L is substituted with M in TRS (Figures 3A, 3E and 3G). In the structure, residue Met60 plays a critical role in the interaction with 4EHP, by fitting snugly into the hydrophobic pocket formed by Val91, Phe94, Trp95, Leu153, and Leu156 of 4EHP (Figure 3G). Meanwhile, residue Leu617 in eIF4G and Leu59 in 4E-BP1, corresponding to Met60, only form hydrophobic interactions with Trp73, Leu135, and Ile138 in eIF4E, as does Leu59 in 4E-BP1 with Leu56, Val91, Leu153, and Leu156 in 4EHP (Figure 3G). In the structure of the *Drosophila melanogaster* eIF4E and Thor (an ortholog of vertebrate 4E-BP) complex, Thor also utilizes a methionine in the L consensus sequence. However, Thor Met59 shares the interaction pattern observed in eIF4G Leu617 and 4E-BP1 Leu59 with eIF4E and 4E-BP1 Leu59 in 4EHP. Specifically, this residue forms hydrophobic interactions with Leu72, Val102, Leu117, and Ile170 of eIF4E (23). Another example of a protein that also includes a methionine in the latter consensus sequence is GIGYF2 that interacts with murine 4EHP to form an essential complex for mammalian development (16). However, structural information on this complex is not yet available.

Mutations at Tyr55 and Met60 in the consensus sequence of TRS completely abolished co-immunoprecipitation with 4EHP, confirming their pivotal roles in interacting with 4EHP (Figure 3H). In contrast, mutations at Tyr53 and Ile63 showed no and mildly reducing effects on the interaction with 4EHP, respectively (Figure 3H). These results are supported by the structure in which Ile63 contributes to hydrophobic interactions with His54, Val91, and Trp95 of 4EHP while Tyr53 is exposed to bulk solvent and is only marginally involved in the interaction with 4EHP (Figure 3F). Mutations of 4EHP at His54, Phe94 and Leu156 completely abolished co-precipitation with TRS (Figure 3I). The TRS M60K mutant retained the catalytic activity (Figure 4A) but lost its ability to bind to 4EHP (Figures 3H and 4B). Conversely, the TRS C413S mutant lost its catalytic activity (Figure 4C) but could still bind to 4EHP (Figure 4B). These results suggest that the 4EHP-binding activity of TRS does not require its catalytic activities, and the reverse is also true.

Interaction between 4EHP and TRS as a gain of function in vertebrates

To further understand the functional implication for the TRS and 4EHP complex formation, this complex formation was investigated in different species. While the catalytic domain of TRS is highly conserved throughout the three kingdoms, a BLAST search revealed that the UNE-T region is shared only among eukaryotic TRSs (from yeast to human). In addition, 4EHP has been found in metazoans (13, 29). Thus, TRS-4EHP interaction is unique to metazoans. Analysis of the 4EHP-interacting -helix-forming region revealed that mouse and zebrafish TRSs share similar amino acid sequences with human TRS, while fly TRS shows difference (Figure 5A). Besides, mouse and

12

zebrafish 4EHPs are particularly similar in the region containing the H-P-L motif critical for TRS binding in human case, while fly 4EHP is less similar (Figure 5A). Co-immunoprecipitation showed the potential interaction of TRS and 4EHP in mouse (Figure 5B). Zebrafish TRS (zTRS) and 4EHP (z4EHP) also showed the interaction, and mutations at the residues Asp50 and Ile55 of the canonical eIF4E-binding residues (corresponding to tyrosine and leucine, respectively, in the YX_4L motif) markedly reduced the interaction with 4EHP (Figure 5C). However, the pairs of fly TRS (dTRS) with either fly 4EHP (d4EHP) or human 4EHP did not show the interaction (Figure 5D). To further confirm these results, the pairs of GST-4EHP and HA-TRS from same species (human, fish and fly), or the pair of fly TRS and human 4EHP in *E. coli* were co-expressed. When the pairwise interactions were tested by *in vitro* pull-down of the cell lysates using Ni-affinity chromatography, the pairs of human, fish and fly showed the strongest, modest and no interaction, respectively, as determined by Coomassie staining of the eluted proteins from the column beads (Figure 5E). These results suggest the vertebrate-specific emergence of the TRS-4EHP interaction.

eIF4G-like function of TRS

Structural homology of the TRS-4EHP complex to other translational initiation complexes led to hypothesize a potential regulatory role of TRS in translation initiation. To validate this possibility, the interaction of the two protein and its dependency on m^7GTP cap was examined. Since 4EHP binds to the 5´-cap structure (22, 30), the possible involvement of TRS in the cap structure was investigated using the 5´ UTR cap analog m^7GTP-bound endogenous 4EHP in

different cell lines. The cap-bound endogenous proteins were eluted from m^{7}GTP-Sepharose beads and immunoblotted with TRS and 4EHP antibodies. The results showed the association of TRS with m^{7}GTP-bound 4EHP, but not with Sepharose beads (Figure 6A). Myc-TRS WT, but not the 4EHP-binding defective TRS M60K mutant, showed the interaction with HA-4EHP only in the presence of m^{7}GTP-Sepharose beads (Figure 6B). Conversely, TRS showed association with 4EHP WT only in the presence of m^{7}GTP-Sepharose beads, but not with the TRS-binding defective 4EHP triple mutant H54N/F94W/L156K (HFL; Figure 6C). Combined together, the pairwise interactions between TRS and 4EHP and also between 4EHP and 5`-cap appear to facilitate with each other.

The eIF4G and eIF4E are known to form the active eIF4F translation initiation complex with eIF4A. Since TRS interacts with cap-bound 4EHP, pull-down assay was evaluated whether it would also bind to eIF4A and eIF4G. Strep-TRS showed the interaction with FLAG-eIF4A, but not with eIF4G (Figure 6D). The interaction between TRS and eIF4A was still maintained in the absence of 4EHP, even when the interaction of TRS and 4EHP was disrupted by mutations (Figure 6E). These results suggest that the interaction of TRS with eIF4A may occur regardless of the interaction between TRS and 4EHP. Co-immunoprecipitation of 4EHP with different functional domains of TRS determined that the TGS and editing domain (TGS/ED) and the anticodon-binding domain (ABD) of TRS are responsible for the interaction with eIF4A (Figure 6F).

Combined together, TRS appears to interact with cap-bound 4EHP and eIF4A, but not with eIF4G, and the interaction with eIF4A is independent of 4EHP. Indeed, it is known that 4EHP does not interact with eIF4G (13, 31). Based on these results, it was speculated that

14

TRS may function as a mediator in the formation of a vertebrate-specific eIF4F-like complex (hereinafter referred to as V-eIF4F) together with 4EHP and eIF4A, similarly to eIF4G in the eIF4F complex. To assess the complex specificity of the factors, TRS or 4EHP was suppressed and monitored how depletion of these factors affected precipitation of the others. When TRS was silenced eIF4G, eIF4E, and eIF4A components of the eIF4F complex were pulled down with m^7GTP-Sepharose, and a small amount of 4EHP was still detected, perhaps due to its intrinsic affinity for the m^7GTP cap (Figure 6G). When 4EHP was suppressed, however, only the eIF4F components were detected at significant levels (Figure 6G). Next, the effects of eIF4G and eIF4E suppression on the formation of the TRS-mediated complex were examined. When eIF4G or eIF4E was suppressed, TRS and 4EHP were mainly detected with the cap (Figure 6H), and a small amount of eIF4E was again detected. It should be noted that eIF4E binds to the cap analog m^7GTP with approximately 100-fold greater affinity than 4EHP (30). Since eIF4A is commonly present in both of the TRS-4EHP and eIF4E-4G complexes, suppression of either complex showed only a porteion of eIF4A remained bound to the other intact complex (Figure 6G and 6H). All of these results indicate that the TRS-mediated translation initiation complex is formed independently of the eIF4F complex.

  The poly(A)-binding protein (PABP) interacts directly with eIF4G to facilitate translation initiation of polyadenylated mRNAs (32, 33). Pull-down assays clearly showed that TRS interacts with PABP in addition to 4EHP and eIF4A (Figure 6I). Co-precipitation showed the interaction of FLAG-PABP with both of TRS WT and the 4EHP-binding defective M60K mutant, indicating that the interaction of the two proteins is independent of 4EHP (Figure 6J). To see how

the suppression of TRS, 4EHP, eIF4A or eIF4G would affect global translation, each of these factors was knocked down with their specific siRNAs and the cell lysates were immunoblotted with anti-purocymin antibody as previously described (34). Suppression of these factors except for eIF4G gave little effect on global translation at least in this experimental conditions (Figures 7A and 7B). Although it is not clear why global translation was affected only by eIF4G suppression at this moment, the similar results were also previously reported (35, 36).

 Taken together, these results propose a schematic model of TRS-mediated translation initiation machinery by analogy to the eIF4F complex (37, 38). The TRS UNE-T helix binds to the initiation factor 4EHP that recognizes the 5′-cap of mRNA and the TRS catalytic part acts as a scaffold to recruit eIF4A and poly(A)-bound PABP to form eIF4F-like complex (Figure 6K).

Functional implication of the TRS and 4EHP complex

The results so far demonstrated that TRS-mediated V-eIF4F complex formation is unique to vertebrate lineage. To understand biological functions of this complex in vertebrate translational control, RNA-immunoprecipitation experiments were performed with rabbit anti-TRS antibody, and with rabbit IgG and anti-AlaRS antibody for comparison, followed by deep sequencing (RIP-seq) (Figure 8A). TRS was targeted for the RIP-seq experiments because it would be a determinant for the specificity of V-eIF4F-binding mRNAs. In contrast to TRS, 4EHP is known to regulate translation initiation of different mRNAs for mammalian development (16) and oxygen-regulated protein expression (11).

 2,928 transcripts enriched in anti-TRS immunoprecipitate were

identified, a functional annotation clustering analysis was performed using the Database for Annotation, Visualization and Integrated Discovery (39) and classified by gene ontology (GO) term in the biological process categories (Figure 8B). The results showed that 39.8, 18.1 and 13.9% of the 166 enriched GO terms are related to system development, cellular metabolic process and nitrogen compound metabolic process, respectively. Interestingly, most of the genes in the system development group appear to reflect biological processes that are unique to vertebrates and presumably important during the invertebrate-to-vertebrate transition (30.3, 13.6, 13.6 and 9.1% belong to the development of nervous system, skeletal system, circulation system and tube formation, respectively) (Figure 8C).

Among the TRS-enriched transcripts, over-represented genes were noticed involved in vasculogenesis and/or angiogenesis since it is considered as one of the evolutionary hallmarks for vertebrates. During this process, mesodermal cells differentiate into endothelial precursor cells (angioblasts) to form the earliest vessels. Angioblasts migrate and differentiate in response to local cues (such as growth factors) to form new blood vessels, and these blood vessels further grow through angiogenesis. RIP-seq data analysis suggested that TRS would interact with the 5′UTR of mRNAs for angiogenic factors.

Next, it is investigated how TRS-mediated V-eIF4F complex could select its target mRNAs. For this, it is referred to a previous report that *E. coli* TRS can selectively bind to its own mRNA for auto-translational repression by binding to 5' UTR (20). The crystal structure of TRS catalytic and anticodon-binding domains complexed with the essential region of 5' UTR revealed that the mRNA region forms an anticodon-like loop and interacts with the TRS

anticodon-binding domain, in a mode mimicking tRNA anticodon binding (20). The catalytic and anticodon-binding domains of TRS are highly conserved among different species and the residues responsible for binding to the mRNA anticodon-like loop in *E. coli* TRS (*e.g.*, Arg583, Glu600, and Arg609) are strictly conserved with those in human counterpart (*e.g.*, Arg428, Glu680, and Arg689). It could be therefore predicted that human TRS may interact with mRNAs in a similar mode to *E. coli* TRS. To validate hypothesis, potential loop structures located at the 5′ UTR of the vascular endothelial growth factor (VEGF) mRNA were searched using RNA structure prediction (40), and the potential loop structures were identified containing anticodon-like base triplets UGU for threonine codon at the positions of -167 and -749from the VEGF mRNA initiation codon AUG, respectively (Figure 8D). To validate whether these are the sites responsive to the TRS-mediated initiation complex, two different 5' UTR regions were fused containing each of the anticodon-like base triplets (5′ UTR-167 and 5′ UTR-749) to the upstream of luciferase gene, and expressed in TRS- or AlaRS-expressing 293T cells (Figure 8D). The luciferase gene expression was increased from 5′ UTR-167, but not from 5′ UTR-749, in the control 293T cells and further increased in TRS-expressing, but not in AlaRS-expressing 293T cells (Figure 8D). Furthermore, mutations of the pseudo-anticodon located in the stem-loop diminished translation of the reporter gene (Figure 8E). Translation of the reporter construct containing 5′ UTR-167 was markedly decreased in siTRS-transfected 293T cells, but not in siAlaRS-transfected cells, further supporting the specificity of TRS for the translation of the reporter protein from 5′ UTR-167 (Figure 8F). Human TRS contains Arg428, Glu680, and Arg689 (RER) that

are predicted to be involved in the interaction with the pseudo-anticodon of VEGF mRNA based on the homology to *E. coli* TRS (20). It is checked how mutations of these residues would affect the translation of the reporter gene. Translation of the reporter gene was increased in the WT TRS-expressing cells, but not in the mutant TRS-expressing cells (Figure 8G). Combined together, these results suggest that V-eIF4F may regulate the translation of VEGF mRNA via the interaction of TRS anticodon-binding domain with the pseudo-anticodon in 5'UTR region.

Vertebrate-specific translational control of angiogenesis via the TRS and 4EHP complex

Since the results above suggested the potential role of V-eIF4F complex in blood vessel formation, its functional significance was tested in cell and *in vivo*. Suppression of TRS or 4EHP using their specific siRNAs significantly reduced VEGF at the protein level (Figure 9A), while little changes at VEGF mRNA levels (Figure 9B). Similar results were also obtained with angiogenin (ANG) (Figures 9C and 9D), mRNA of which were also over-represented in the RIP-seq analysis with TRS. The levels of secreted VEGF and ANG were also measured in various cell lines, and markedly diminished levels of VEGF (Figure 9E) and ANG (Figure 9F) in either or both of TRS and 4EHP-suppressed cells. All of these results suggest that the V-eIF4F complex would positively regulate translation of angiogenic factors via TRS and 4EHP.

 Next, it is evaluated whether TRS- and 4EHP-regulated translation would show any effects on endothelial cell migration and vessel (tube) formation using human umbilical vein endothelial cells

19

(HUVEC). For these experiments, embryonic lung tissue-derived WI-26 cells were treated with anti-TRS and/or anti-4EHP siRNA, and the culture supernatants of the transfected cells were used for the assays. The supernatants from siTRS- and/or si4EHP-WI-26 cells showed the decreased activities in the induction of tube formation compared with those from siCont- or VEGF-treated cells (Figures 10A and 10B). The supernatants from siTRS- and/or si4EHP-treated WI-26 cells also exhibited lower activity in endothelial cell migration than those from siCont- or VEGF-treated cells (Figure 10C). Similar effects on endothelial cell migration and tube formation were also observed in 293T cells (Figures 10D-10F). The tube formation activities of HUVEC were enhanced by the supernatants from ectopically WT TRS expressing WI-26 cells (Figures 10G and 10H), but not from 4EHP-binding defective TRS (M60K)-expressing cells (Figures 10G and 10H). In addition, migration assays demonstrated that disruption of the 4EHP-TRS interaction (in the TRS M60K variant) reduced endothelial cell migration, while recovery of the interaction (WT TRS) enhanced cell migration (Figure 10I). Since TRS itself can be secreted to induce angiogenesis (41), the secretion of TRS WT and M60K mutant to the culture media was checked and observed that both were secreted to the similar amounts (Figure 10J), indicating that the different angiogenesis inducing activities of the TRS WT- and M60K mutant-expressing cells did not result from the different amount of the secreted TRS.

 The TRS- and 4EHP-mediated translation of angiogenesis-related mRNAs were further explored in zebrafish model representing a closed circulatory system that is a characteristic of vertebrates. The formation of stereotypical central arteries (CtAs) was examined in the developing hindbrain of zebrafish embryos at 52 h post-fertilization

20

(hpf) (Figure 11A). The involvement of TRS or 4EHP in angiogenesis and their interaction *in vivo* were assessed by generating a transiently abnormal interaction via knockdown of TRS or 4EHP using splicing-blocking morpholinos (MOs). While the morpholino treatment significantly suppressed the normal transcript generation of 4EHP, it was only moderately blocked in the case of TRS even after trial of a few different combinations of primers for unknown reason (Figures 11B and 11C). Nonetheless, suppression of TRS (*trs* MO + Cont RNA) reduced CtA length and branching points by 19 and 30%, respectively, compared with control (Cont MO + Cont RNA) (Figures 12A–12C). Defective angiogenesis upon TRS suppression was rescued by expression of WT TRS (*trs* MO + *trs* RNA), but not by expression of the 4EHP interaction-defective I55D mutant (*trs* MO + I55D RNA) (Figures 12A–12C). Similarly, 4EHP suppression (*4ehp* MO + Cont RNA) reduced 22% and 34% in CtA length and branching points, respectively, and these defects were also rescued by expression of4EHP (*4ehp* MO + *4ehp* RNA) (Figures 12D –12F). In addition, several angiogenic defects including vessel shortening and mis-sprouting of intersegmental vessels (ISVs) in the trunk of zebrafish embryos at the same stage were also observed upon 4EHP suppression (Figure 11D). Taken together, these results suggest that the 4EHP-TRS interaction-mediated V-eIF4F complex positively regulates protein synthesis from a subset of mRNAs that are crucial for vascular development.

Figure I-1. TRS specifically interacts with 4EHP
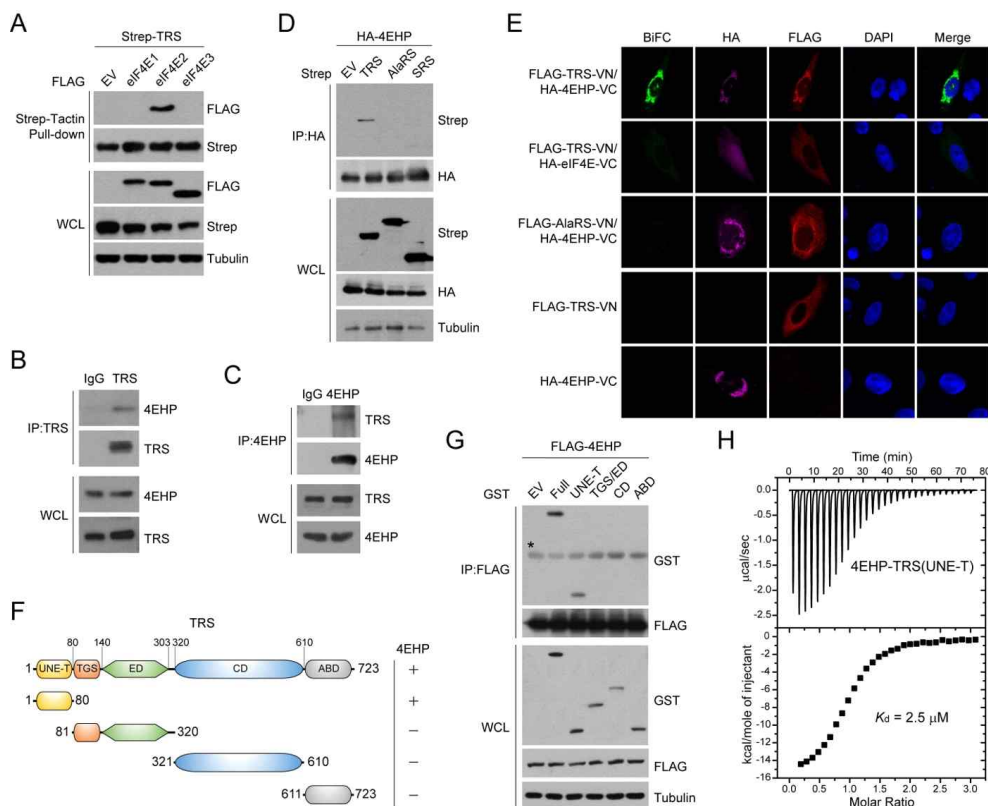
(A) Strep-tagged human TRS was co-expressed with each of FLAG-eIF4E isoforms in 293T cells. Strep-TRS was pulled down with Strep-Tactin beads and co-precipitates were analyzed by immunoblotting with anti-FLAG antibody. EV, empty vector; WCL, whole cell lysates.

(B) Endogenous TRS was immunoprecipitated with anti-TRS antibody in WI-26 cell lysates and co-immunoprecipitation of endogenous 4EHP was determined by anti-4EHP antibody.

22

(C) Co-immunoprecipitation of the two proteins above was also confirmed in reverse order. Rabbit IgG was used as a negative control.

(D) HA-4EHP was co-expressed with each of human TRS, alanyl-tRNA synthetase (AlaRS) and seryl-tRNA synthetase in 293T cells, immunoprecipitated with anti-HA antibody from cell lysates, and co-immunoprecipitation was determined by immunoblotting with anti-Strep antibody.

(E) Interactions of the indicated protein pairs were determined by reconstitution of Venus green fluorescence protein in CHO cells. The nuclei were stained by DAPI (blue). Expression of HA-4EHP and FLAG-TRS was confirmed by immunofluorescence staining with anti-HA (Alexa 647) and anti-FLAG (Alexa 594) antibodies, respectively. Bottom two panels show the cells expressing TRS or 4EHP only. VN, Venus N-domain; VC, Venus C-domain.

(F) Domain structure of human TRS. The domain structure was determined based on the crystal and solution structures of the *E. coli* (PDB 1QF6) and human (PDB 1WWT) TRSs, respectively. UNE-T, unique domain extension at the N-terminus of TRS; TGS, a domain named after TRS, GTPase, and SpoT; ED, editing domain; CD, catalytic domain; ABD, anticodon-binding domain.

(G) FLAG-4EHP was co-expressed with each of GST-TRS full-length and the indicated domains in 293T cells. Cell lysates were immunoprecipitated with anti-FLAG antibody, and co-precipitated

TRS domain(s) was determined by immunoblotting with anti-GST antibody. The asterisk (∗) indicates the position of the IgG heavy chain.

(H) Isothermal titration colorimetry was carried out to determine the binding affinity and stoichiometry of TRS UNE-T region to 4EHP. Raw data and integration plot are displayed in the upper and lower panel, respectively.

Figure I-2. Overall structure of TRS (UNE-T) bound to 4EHP
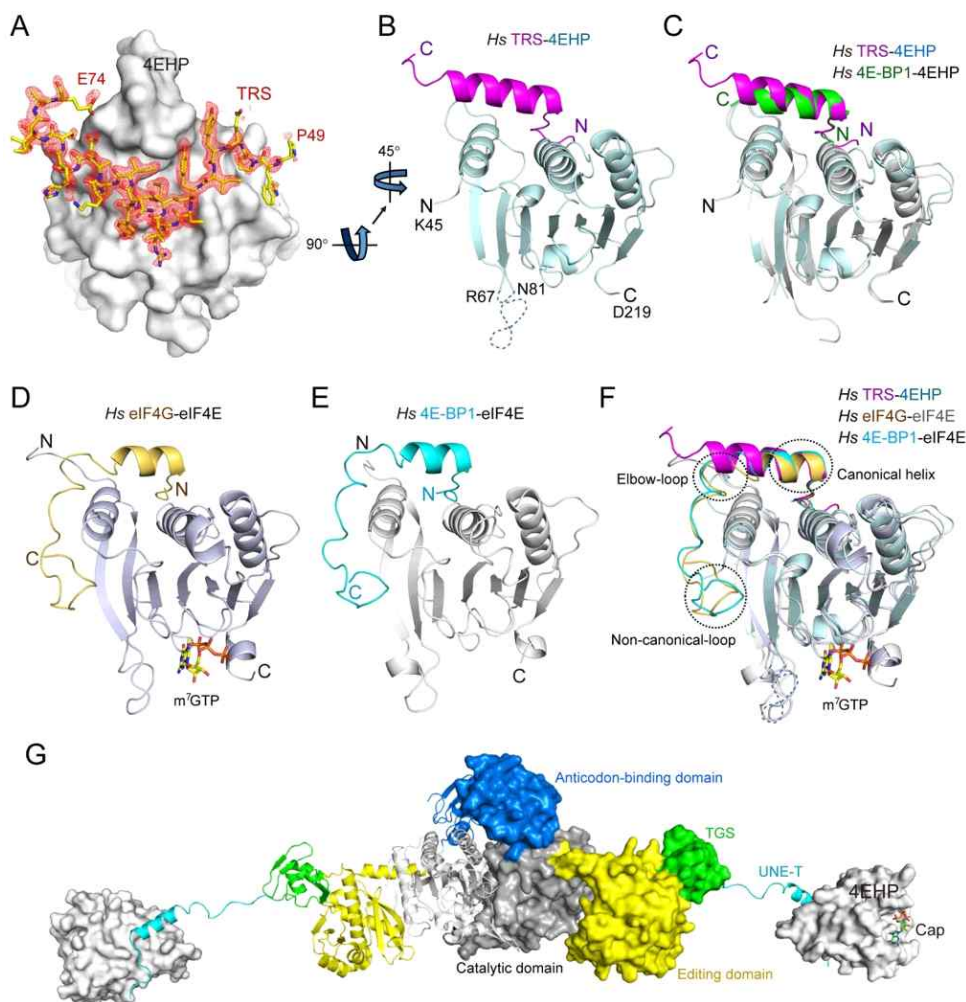
(A and B) Structure of the TRS (UNE-T)-4EHP complex. (A) 4EHP is displayed using surface representation, while TRS (UNE-T) is shown in stick representation. The F_o-F_c electron density map of TRS (UNE-T) was calculated before the inclusion of TRS (UNE-T), and is contoured at 2.5 s. (B) Cartoon representation of the TRS

(UNE-T, magenta) and 4EHP (pale cyan) complex. *Hs*, *Homo sapiens*.

(C) Superimposition of the TRS-4EHP structure (magenta and pale cyan) onto the 4E-BP1-4EHP structure (green and gray).

(D and E) Cartoon representations of the eIF4G (dark yellow)-binding eIF4E (light blue) and the 4E-BP1 (cyan)-binding eIF4E (gray). (D) The m^{7}GTP cap analog bound to eIF4E is shown in stick representation.

(F) Superimposition of the structures of eIF4G and 4E-BP1 bound to eIF4E, and TRS bound to 4EHP.

(G) Structural model showing how 4EHP could interact with the UNE-T region of each subunit of the TRS dimer (colored light teal and cyan, respectively). Each domain of TRS is labeled as in Figure 1F. The model was built based on the crystal structure (PDB1QF6) of the *E. coli* TRS (46).

Figure I-3. Surface representation of the TRS-binding interface of 4EHP
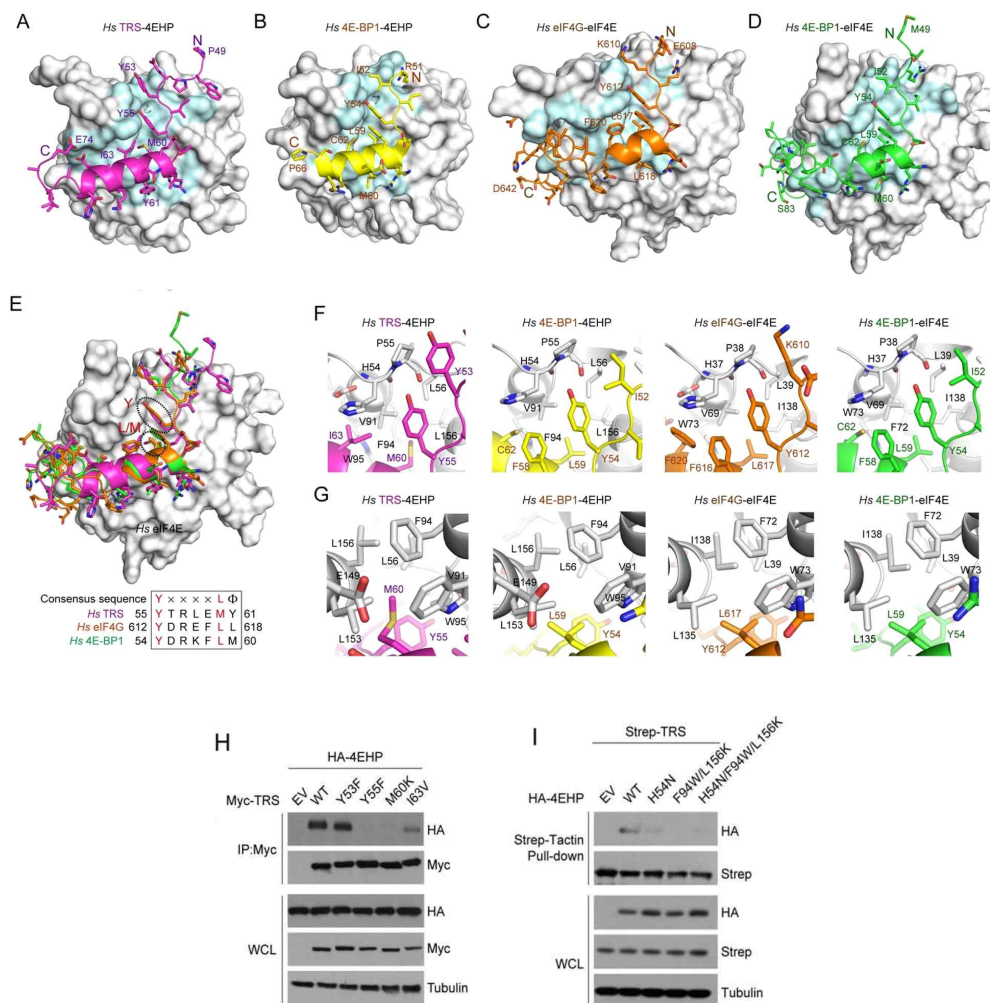
(A and B) The TRS (magenta) and 4E-BP1 (yellow) residues involved in the interaction with 4EHP are shown in stick representation. Surface regions colored pale cyan represent 4EHP residues responsible for the interaction with TRS and 4E-BP1.

(C and D) The eIF4G (bright orange) and 4E-BP1 (green) residues involved in the interaction with eIF4E are shown in stick representation. Surface regions colored pale cyan represent eIF4E residues responsible for the interaction with eIF4G and 4E-BP1.

(E) Interaction between TRS and 4EHP is mediated by the canonical eIF4E-binding motif. TRS, eIF4G, and 4E-BP1 are superimposed on the eIF4E surface structure for comparison. Y and L/M of the consensus sequences are highlighted by black dotted circles. Sequence alignment of the eIF4E-binding consensus motif is shown.

(F) Features of the TRS Tyr55 interaction with 4EHP are conserved with those of the 4E-BP1 Y54 complexed with 4EHP, and the eIF4G Y612 and 4E-BP1 Y54 complexed with eIF4E.

(G) Features of the TRS Met60 interaction with 4EHP are distinct from those of the 4E-BP1 L59 complexed with 4EHP, and eIF4G L617 and 4E-BP1 L59 complexed with eIF4E.

(H) Myc-TRS wild-type (WT) or mutant was co-expressed with HA-4EHP in 293T cells. Myc-TRS was immunoprecipitated with anti-Myc antibody and co-precipitated 4EHP was determined by immunoblotting with anti-HA antibody. EV, empty vector; WCL, whole cell lysates.

(I) HA-4EHP WT or mutant was co-expressed with Strep-TRS. Strep-TRS was pulled down with Strep-Tactin beads, and co-precipitated 4EHP was determined by immunoblotting with anti-HA antibody.

Figure I-4. Relationship between the 4EHP-binding and catalytic activity

(A) The catalytic activities of TRS WT and 4EHP-binding defective M60K (50 nM) mutant (A) were determined by threonylation of tRNA^{Thr} as described in Methods. The amounts of the threonine-charged tRNA were measured by scintillation counting and the data (mean± SEM of three experiments) were displayed as line graphs. c.p.m, count per minute.

(B) HA-4EHP was co-expressed with each of Myc-TRS WT, M60K and C413S mutants in 293T cells. TRS was immunoprecipitated with anti-Myc antibody and co-precipitation of HA-4EHP was determined by immunoblotting with anti-HA antibody. EV, empty vector; WCL, whole cell lysates.

(C) The catalytic activities of TRS WT and the catalytic inactive C413S mutant were also compared as described above.

Figure I-5. The TRS-4EHP interaction represents an evolutionary gain of function in vertebrates
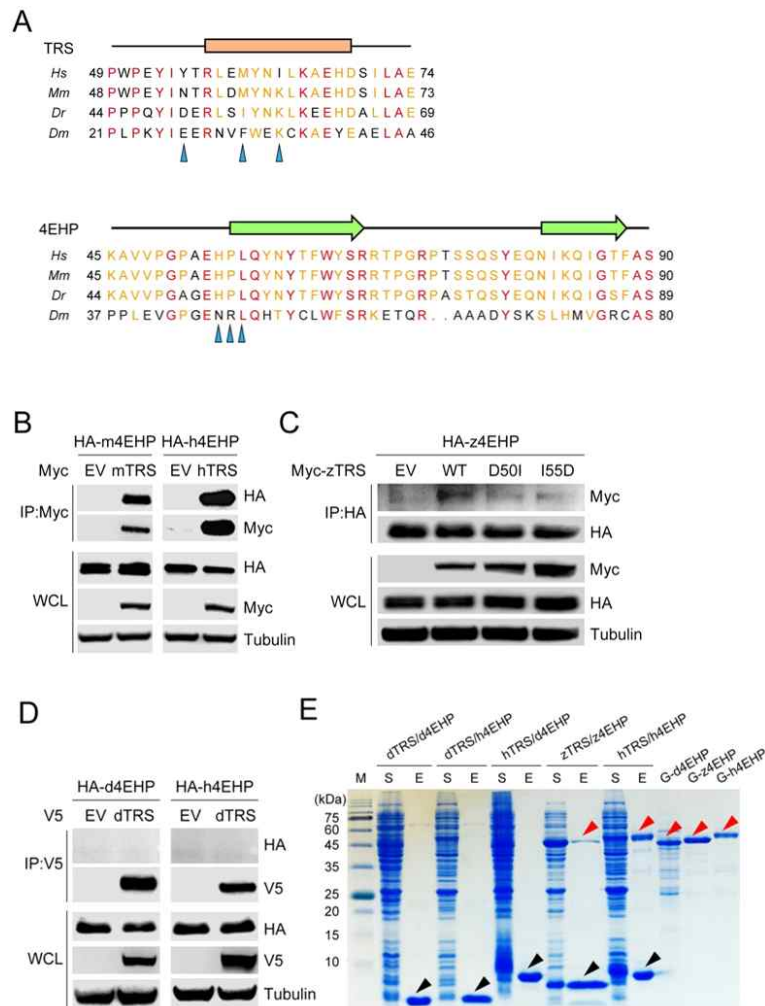
(A) Structure-based sequence alignment of TRS and 4EHP in different species. Residues critical for the interaction between TRS and 4EHP are indicated by blue arrowheads. *Hs*, *Homo sapiens*; *Mm*, *Mus musculus*; *Dr*, *Danio rerio*; *Dm*, *Drosophila melanogaster*.

(B) The indicated pairs of human (h) and mouse (m) Myc-TRS and HA-4EHP were expressed in 293T cells. Myc-TRS was immunoprecipitated with anti-Myc antibody and co-precipitation of HA-4EHP was determined by immunoblotting with anti-HA antibody. EV, empty vector; WCL, whole cell lysates.

(C) Interaction of zebrafish Myc-TRS WT or mutant with HA-4EHP was also determined as above.

(D) Fly HA-4EHP (d4EHP) or h4EHP was expressed with fly V5-TRS (dTRS) in *Drosophila* S2 cells. V5-TRS was immunoprecipitated with anti-V5 antibody and co-immunoprecipitation of HA-4EHP was determined by immunoblotting with anti-HA antibody.

(E) The pairs of HA-TRS (UNE-T) and GST-4EHP from the indicated species were co-expressed in *E. coli.* HA-TRS was pulled down with Ni-NTA resin, and co-precipitated GST-4EHP was eluted from the resin and detected by Coomassie staining. M, molecular size marker; S, soluble fraction containing the proteins expressed in *E. coli* BL21 (DE3); E, proteins eluted from the Ni-NTA resin. Black and red arrowheads indicate His-TRS (UNE-T) and GST-4EHP, respectively.

Figure I-6. TRS functions similarly to eIF4G to form an eIF4F-like complex
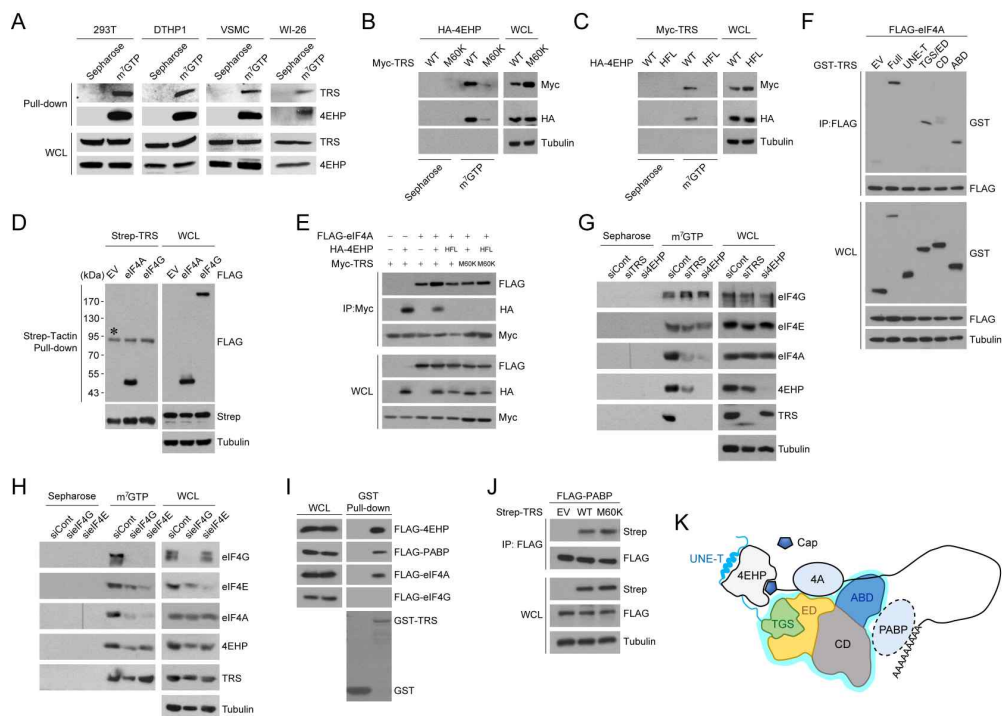
(A) Cap structure-binding assay of endogenous 4EHP and TRS in 293T, differentiated THP1 (DTPH1), VSMC, and WI-26 cell lysates. Equal amounts of total extracted proteins were incubated with Protein A-Sepharose or cap analog m^7GTP-Sepharose, followed by immunoblotting with anti-TRS and -4EHP antibodies. WCL, whole cell lysates.

(B) Myc-TRS WT TRS or M60K mutant was co-expressed with HA-4EHP in 293T cells and subjected to cap structure-binding assays as above.

(C) HA-4EHP WT or HFL mutant was co-expressed with Myc-TRS in 293T cells, and subjected to cap structure-binding assays as above. HFL, 4EHP (H54N/F94W/L156K) triple mutant.

(D) Strep-TRS was co-expressed with FLAG-eIF4A or -eIF4G in 293T cells. Strep-TRS was pulled down with Strep-Tactin beads and co-precipitation of eIF4A or 4G was determined by immunoblotting with anti-FLAG antibody. EV, empty vector. The asterisk (*) indicates a nonspecific band detected by western blot of precipitated samples with anti-FLAG antibody.

(E) Different combinations of the indicated proteins were expressed in 293T cells and TRS was immunoprecipitated with anti-Myc antibody and co-precipitation of other proteins were determined by their tagged antibodies.

(F) FLAG-eIF4A was co-expressed with GST-TRS full-length or the indicated domains in 293T cells. FLAG-eIF4A was immunoprecipitated with anti-FLAG antibody, and co-precipitated TRS proteins were determined by immunoblotting with anti-GST antibody.

(G) 293T cells were transfected with siRNAs against TRS, 4EHP, or a non-targeting control (siCont) for 48 h. Cell lysates were incubated with m^7GTP-Sepharose beads. Cap-bound proteins were eluted from beads and immunoblotted with the indicated antibodies. Protein A-Sepharose beads were used as a negative control.

(H) 293T cells were transfected with siRNAs against eIF4G, eIF4E or a non-targeting control (siCont) and the effects of their suppression

on cap-binding of other components were determined as above.

(I) Purified GST-TRS was incubated with each of FLAG-tagged 4EHP, PABP, eIF4A or eIF4G, and their direction interaction with GST-TRS was determined by immunoblotting with anti-FLAG antibody after pull-down with glutathione-Sepharose beads.

(J) FLAG-PABP was co-expressed with each of Strep-TRS WT or M60K mutant in 293T cells, immunoprecipitated with anti-FLAG antibody, and co-precipitated TRS was determined by immunoblotting with anti-Strep antibody.

(K) A schematic model of TRS-mediated translation initiation machinery. TRS UNE-T holds cap-bound 4EHP while N1 and editing domains binds eIF4A. PABP appears to binds a TRS region that is different from the 4EHP and eIF4A binding regions. Although TRS is expected to work a homodimer, the model only shows monomeric model for simplicity.

Figure I-7. Effects of eIF4E, eIF4G, TRS and 4EHP suppression on de novo protein synthesis
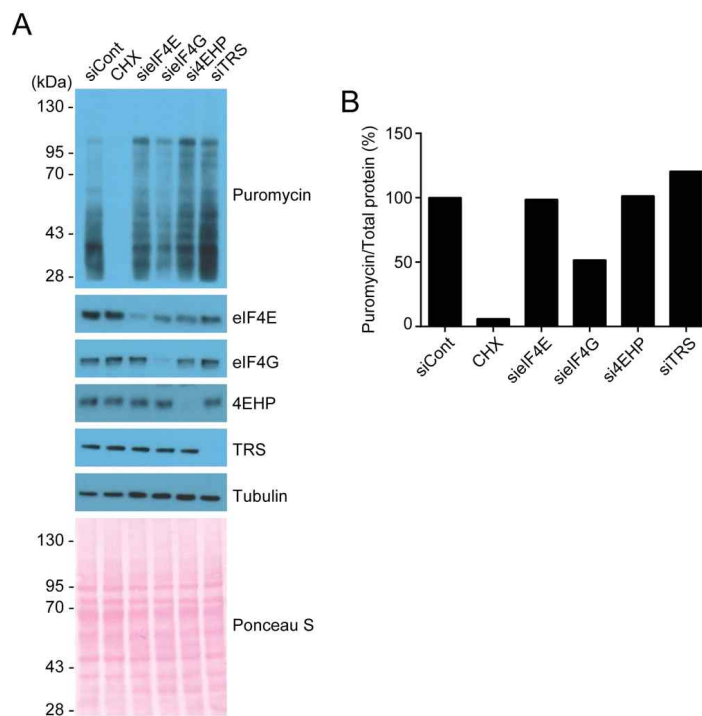
(A) Each of eIF4E, eIF4G, TRS and 4EHP was suppressed with their specific siRNAs for 48 h in 293T cells and treated with puromycin (1 μM) for 30 min. De novo global protein synthesis was then monitored by immunoblotting of cell lysates with anti-puromycin antibody. The whole amounts of cellular proteins were quantified by Ponceau S staining. Cycloheximide (CHX) was employed as positive control to block de novo protein synthesis.

(B) The ratios of de novo protein synthesis versus global protein synthesis were determined as percentage and shown as bar graph.

Figure I-8. V-eIF4F complex-mediated translation initiation control of mRNAs in vertebrates
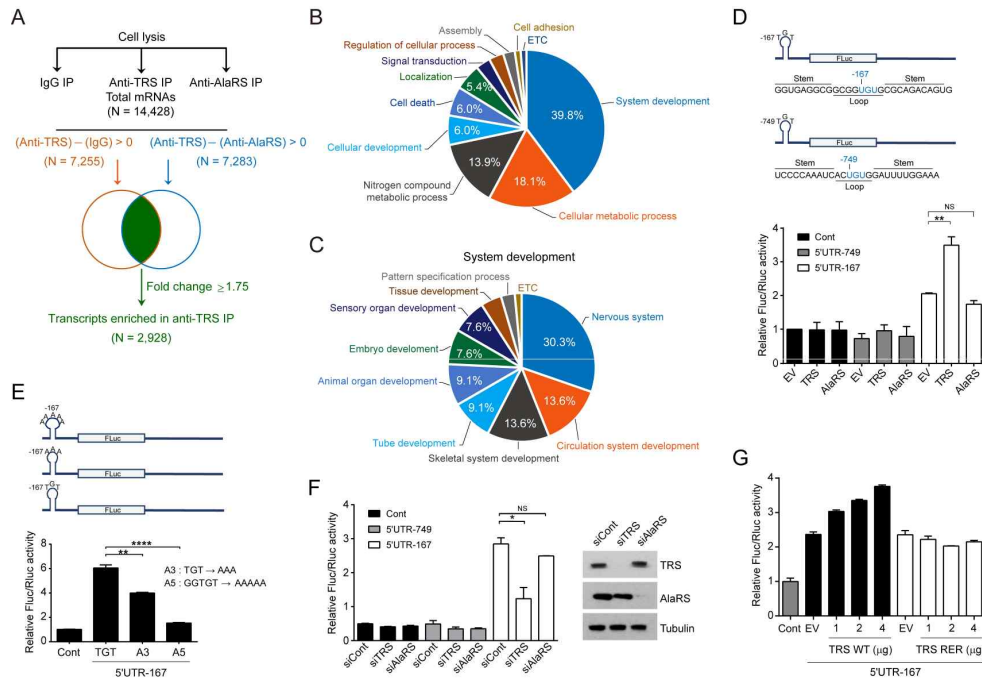
(A) Workflow to identify the TRS-targeted mRNA. Total mRNAs isolated from 293T cells were precipitated with each of anti-TRS, -AlaRS antibodies and mock IgG, and RNA sequencing of the precipitated transcripts was conducted. TRS-enriched RNAs were subtracted by those enriched in AlaRS and also in IgG and the two RNA pools were compared to find the common transcripts.

(B and C) Functional annotation of TRS-associated mRNAs. Enriched GO terms in the biological processes category were analyzed using DAVID.

(D) Potential tRNA^{Thr} anticodon-like stem-loop structures in 5'UTR region of VEGF mRNA. The tRNA^{Thr} anticodon triplet (UGU) was expected at the position of –167 and –749 upstream from the VEGF mRNA initiation codon. The two RNA sequences spanning –1 to –540 and –541 to –1038 bases were fused to the upstream of *firefly* luciferase gene (Fluc), and co-expressed with *Renilla* luciferase gene (Rluc) in TRS- or AlaRS-expressing 293T cells. The data were represented as the ratio of *firefly* to *Renilla* luciferase activity (Fluc/Rluc). Cont, Fluc control vector; EV, empty vector.

(E) Effects of the indicated mutations at the pseudo-anticodon region (-167 site) of VEGF mRNA on translation of the reporter gene were tested in TRS-expressing 293T cells.

(F) Translation of the pseudo-anticodon (-167 site) containing reporter gene were measured in siTRS- or siAlaRS-transfected 293T cells.

(G) The pseudo-anticodon (-167 site) containing reporter gene was co-expressed with *Renilla* luciferase to monitor TRS-dependent and non-specific translation, respectively. This dual luciferase assay was performed on 293T cells expressing Strep-TRS WT and RER mutant at the indicated dose (1 to 4 mg). RER, TRS (R428L/R680L/R689L) triple mutant. (D, E, and F) *, $p < 0.05$; **, $p < 0.01$; ****, $p < 0.0001$; NS, not significant vs. control group. Values are means ± SEM of three independent experiments.

Figure I-9. Effects of TRS and 4EHP suppression on translation of angiogenic factors
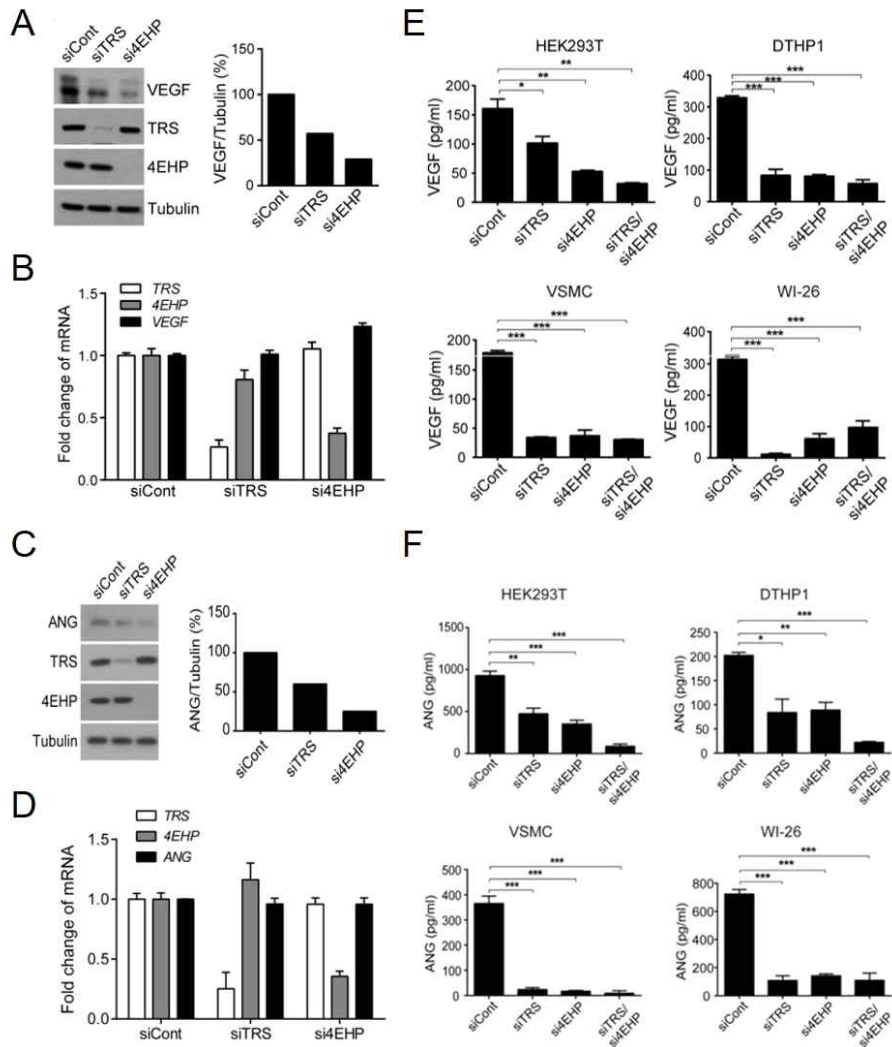
(A) Effects of TRS and 4EHP suppression on cellular protein levels of VEGF were evaluated by immunoblotting in 293T cells (left) and displayed as bar graph after calibration with tubulin levels (right).

(B) Effects of TRS and 4EHP suppression on VEGF transcription were evaluated by qRT-PCR analysis in 293T cells.

(C) Each of TRS and 4EHP was suppressed with their specific siRNAs for 48 h in 293T cells and cellular levels of angiogenin (ANG) were evaluated by immunoblotting with anti-ANG antibody (left) and displayed as bar graph.

(D) Effects of TRS and 4EHP suppression above on the transcript levels of TRS, 4EHP and ANG were analyzed by quantitative RT-PCR with the primers targeting *TRS*, *4EHP*, and *ANG*.

(E) The indicated cells were transfected with siRNAs against TRS, 4EHP, or a non-targeting control (siCont), and the secreted VEGF levels in the culture media were determined by ELISA.

(F) The indicated cells were transfected with siRNAs against TRS, 4EHP, or a non-targeting control (siCont), and the ANG protein levels in the culture supernatants were determined by ELISA against ANG and displayed as bar graphs. (E and F) *, $p < 0.05$; **, $p < 0.01$; ***, $p < 0.001$. Values are means ± SEM of three independent experiments.

Figure I-10. Significance of intracellular TRS and 4EHP in vascular tube formation
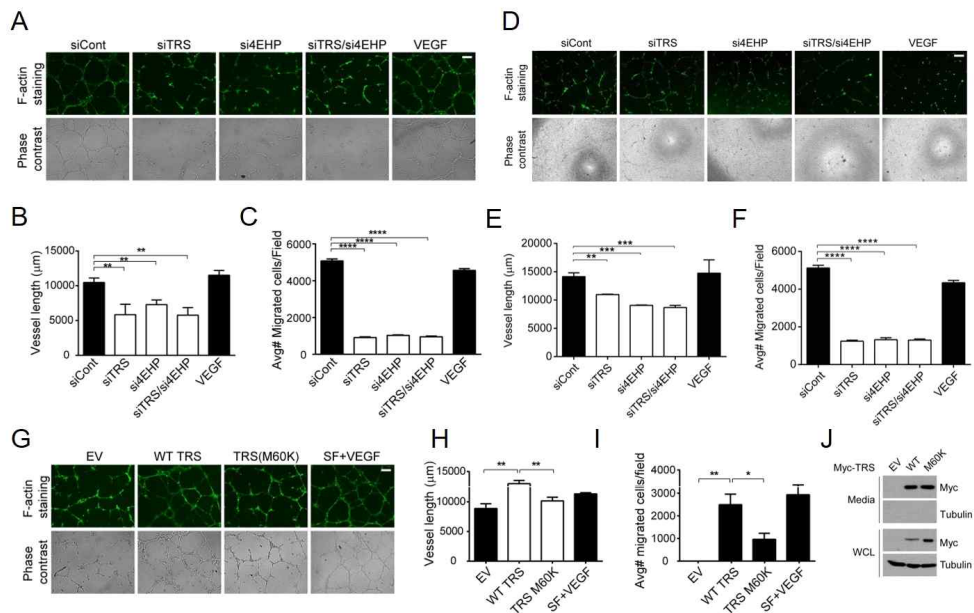
(A) The culture media were prepared from WI-26 cells transiently transfected with siRNAs against TRS and/or 4EHP, or a non-targeting control (siCont). HUVECs with the culture media were then plated on growth factor-reduced Matrigel to form capillary tubes. The cells were stained with anti-F-actin antibody and capillary tube formation in each group was visualized by fluorescence microscopy and also by phase contrast light microscopy. Scale bar = 250 μm.

(B) Total tube lengths in (A) were measure using ImageJ and displayed as bar graph.

(C) Trans-well migration assays were performed on HUVECs above. The migrated cells were counted from randomly picked fields, and averages were calculated.

(D) The culture media were prepared from 293T cells transiently transfected with siRNAs against TRS, 4EHP, or a non-targeting control (siCont). HUVECs treated with these media were then plated on growth factor-reduced Matrigel to form capillary tubes. Capillary tube formation in each group was visualized by immunofluorescence microscopy of F-actin (upper) and also by phase contrast microscopy (lower). Scale bar = 250 μm.

(E) Total tube lengths shown by F-actin immunofluorescence microscopy were quantified using ImageJ and shown as bar graph.

(F) Trans-well migration assays were performed with the culture-media treated HUVECs above. The migrated cells were counted from randomly picked fields of phase contrast microscopy, and the average numbers were shown as bar graph with standard deviation.

(G) The culture media were prepared from WI-26 cells transiently transfected with Myc-TRS WT or M60K mutant. HUVECs treated with the culture media were then plated on growth factor-reduced Matrigel to form capillary tubes. The results were displayed as described above. EV, empty vector. Scale bar = 250 μm.

(H) Total tube lengths in (G) were measure using ImageJ and

displayed as bar graph.

(I) Trans-well migration assays were performed using HUVECs prepared above (G) and measure following the method (F). (B, C, E, F, H, and I) *, p < 0.05; **, p < 0.01; ***, p < 0.001; ****, p < 0.0001. Values are means ± SEM of three independent experiments.

(J) WI-26 cells were transfected with Myc-TRS WT and M60K mutant for 24 h and subsequently incubated in serum-free media for 16 h. The amounts of the secreted and intracellular TRS were compared as described above. EV, empty vector.

Figure I-11. Validation of TRS and 4EHP suppression in zebrafish
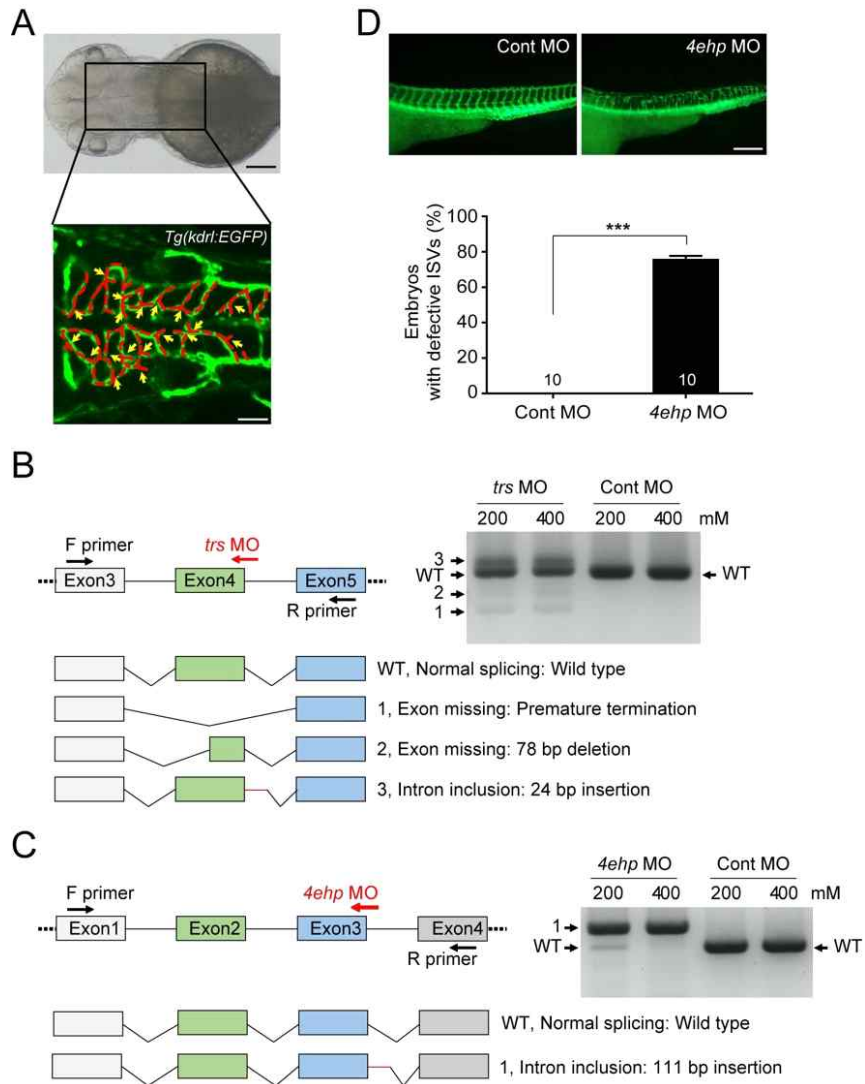
(A) Measurement of angiogenesis of central arteries in the hindbrain of developing zebrafish embryos. (upper) A dorsal view brightfield

image of the brain of zebrafish embryos at 52 hpf (hours post-fertilization). The rectangular region of the Tg(kdrl:EGFP) embryo is the area imaged using a confocal microscopy. (lower) A representative z-projected fluorescent image of Tg(kdrl:EGFP) embryo at 52 hpf. Using this image, the length (red dotted lines) and the branching points (yellow arrows) of CtA vessels were measured and analyzed using ImageJ.

(B) Validation of TRS knockdown by RT-PCR. (upper left) The genomic structure of zebrafish TRS and the locations of the morpholino (MO) blocking the splicing of TRS transcript and primers for RT-PCR. (upper right) RT-PCR to confirm the TRS suppression after injecting the MO. Injection of the MO with different doses (200mM, 400mM) resulted in multiple RT-PCR bands due to the aberrant splicing (bands #1, #2, and #3). Band WT is the normally spliced product from the MO-injected control. (lower) Sequencing of aberrant PCR bands confirmed an out-of-frame mutation (band #1), a partial loss of the exon (band #2), and an insertion of the partial intron due to a cryptic splicing site (band #3) upon *trs* MO injection, suggesting a loss of the normal *trs* function.

(C) Validation of zebrafish 4EHP knockdown by RT-PCR. (upper left) The genomic structure of zebrafish 4EHP and the locations of the MO blocking the *4ehp* splicing and primers for RT-PCR. (upper right) RT-PCR after knocking-down 4EHP with the MO. Injection of the MO with different doses shifted the RT-PCR band due to

aberrant splicing (bans #1). Band WT is the normally spliced product from the MO-injected control. (C) Sequencing of aberrant PCR bands confirmed the introduction of a stop codon due to the intronic insertion (band #1).

(D) Trunk vessel defects upon 4EHP knockdown. (upper) Trunk vessels of the control- (left) and *4ehp* morpholino-treated zebrafish (right) are shown in lateral views. (lower) Angiogenic defects of intersegmental vessels (ISVs) in the developing trunk with high penetrance at 52 hpf in 4EHP suppressed fishes compared to the control. The quantified data are shown in bar graph. ***, $p < 0.001$ vs. control group. Values are means ± SEM, and n values are depicted for each experimental group. Scale bar = 200 μm.

Figure I-12. The 4EHP and TRS interaction is critical for translation initiation of mRNA required for vascular development
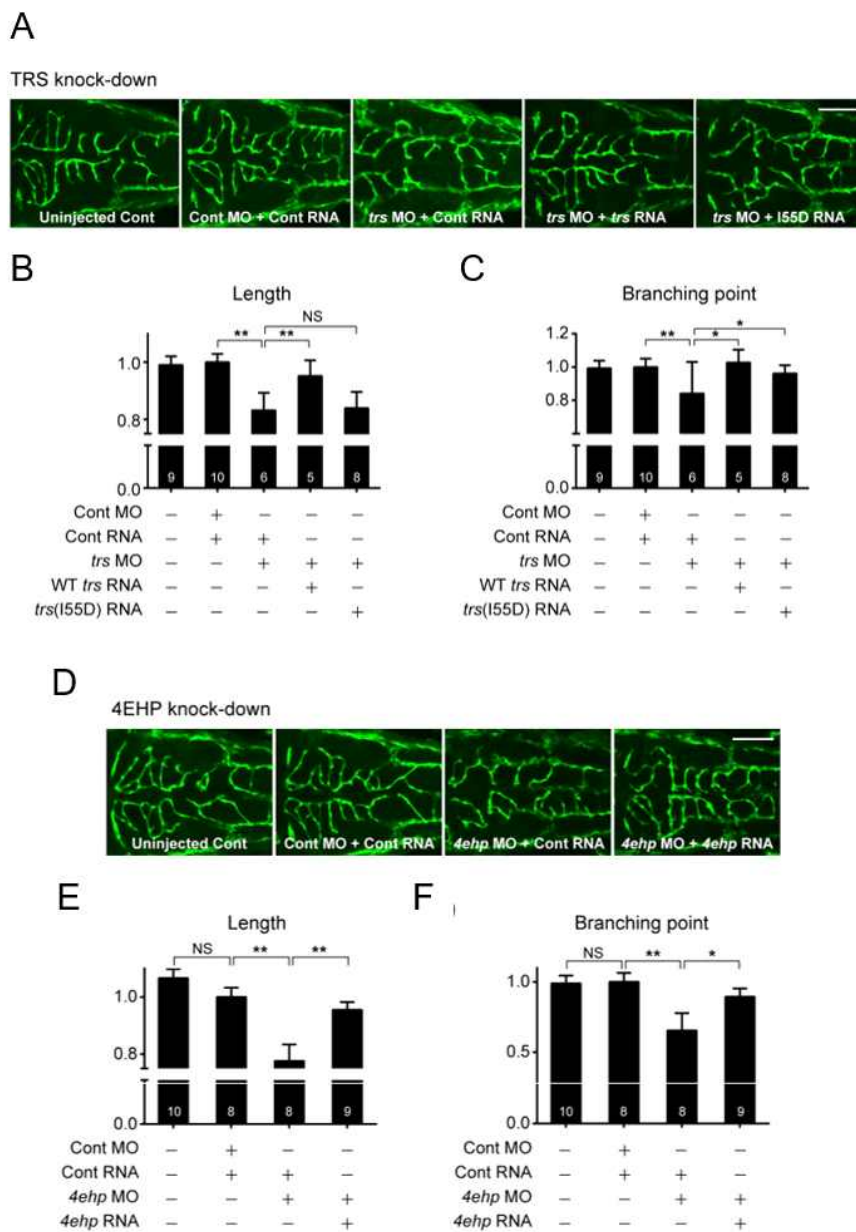
(A‑C) (A) Interaction of TRS and 4EHP promotes angiogenesis *in vivo*. Representative images of the central arteries (CtAs) in the hindbrain of *Tg* (*kdrl:EGFP*) zebrafish embryos of TRS suppression using a morpholino (*trs* MO) together with control (Cont) RNA, or reconstituted with WT or I55D mutant *trs* RNA at 52 h postfertilization.

(D‑F) Representative images of *4ehp* suppression using a morpholino (*4ehp* MO) together with Cont RNA, or reconstituted with WT *4ehp* RNA. Quantitation and statistical analysis of the (B and E) lengths and (C and F) branching points of CtAs. (B, C, E, and F) ∗, $p < 0.05$; ∗∗, $p < 0.01$; NS, not significant vs. control group. Values are means ± SEM, and n values are depicted for each experimental group. Scale bar = 100 µm.

Figure I-13. Changes of cellular levels and transcription of VEGF, TRS and 4EHP at different developmental stages
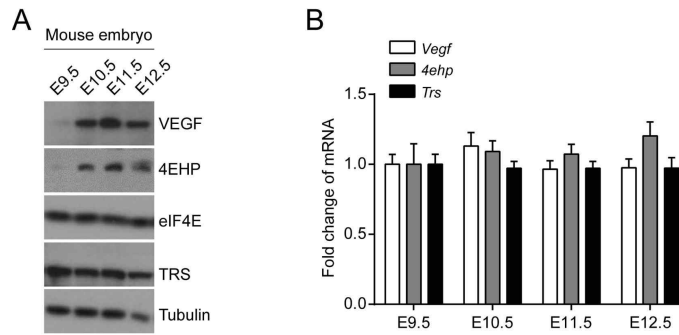
(A and B) (A) Cellular protein and (B) mRNA levels of TRS, 4EHP and VEGF were determined by immunoblotting with their specific antibodies and by RT-qPCR, respectively, in whole mouse embryos at different developmental stages.

Table I-1. Data collection and refinement statistics for complex structure

	TRS (UNE-T)-4EHP complex
Data collection	
Space group	$P2_12_12_1$
Cell dimensions	
a, b, c (Å)	49.37, 60.57, 85.24
α, β, γ (°)	α = β = γ = 90
Wavelength	0.97934
Resolution (Å)	50 - 1.90 (1.97- 1.90)*
No. total reflections	146,691
No. unique reflections	20,718
Redundancy	7.10 (7.10)
Completeness (%)	99.90 (100)
R_{sym} (%)	9.40 (55.30)
$I/\sigma I$	21.10 (13.40)
Refinement	
Resolution (Å)	25.82-1.90
R_{work}/R_{free}	0.16/0.20
R.m.s. deviations	
Bond lengths (Å)	0.007
Bond angles (°)	0.990
No. atoms[a]	
Protein	1,577
Waters	177
Average B-factors (Å^2)	30.80
Geometry (%)	
Favored region	98.00
Allowed region	2.00
PDB accession code	5XLN

*Values in parentheses are for the highest-resolution shell.

[a]Total number of atoms in an asymmetric unit.

Table I-2. Key resources table

Oligonucleotides	Source	Identifier
Non-targeting Control siRNA	Dharmacon	Cat# D-001810
siRNA targeting TRS (SMARTpool)	Dharmacon	Cat# L-011789
siRNA targeting ARS (SMARTpool)	Dharmacon	Cat# L-011565
siRNA targeting EIF4E2 (SMARTpool)	Dharmacon	Cat# L-019870
siRNA targeting EIF4E (SMARTpool)	Dharmacon	Cat# L-003884
Stealth RNAi siRNA Negative Control, Med GC	Thermo Fisher	Cat# 12935300
siRNA targeting EIF4G (Stealth RNAi)	Thermo Fisher	Cat# 10620318
TRS Y55F Forward GTTGAATCCTTGGCCTGAATAT ATTTTCACACGTCTTGAGA	This paper	N/A
TRS Y55F Reverse TCTCAAGACGTGTGAAAATAT ATTCAGGCCAAGGATTCAAC	This paper	N/A
TRS M60K Forward CATGTTCTGCTTTTAGTATAT TATACTTCTCAAGACGTGTGTA AATATATTC	This paper	N/A
TRS M60K Reverse GAATATATTTACACACGTCTT GAGAAGTATAATATACTAAAA GCAGAACATG	This paper	N/A
4EHP H54N Forward GTACTGCAGGGGATTCTCTGCC GGTCCAG	This paper	N/A
4EHP H54N Reverse CTGGACCGGCAGAGAATCCCCT GCAGTAC	This paper	N/A
4EHP F94W Forward TATAAAACCTCCACCACTGCTC CACAGAGGCAAAGGTGCC	This paper	N/A
4EHP F94W Reverse GGCACCTTTGCCTCTGTGGAGC AGTGGTGGAGGTTTTATA	This paper	N/A
4EHP L156K Forward AACCATGAACTGTTCCCCCTTC ATGGCCAAAATGAGATTC	This paper	N/A

50

4EHP L156K Reverse GAATCTCATTTTGGCCATGAAG GGGGAACAGTTCATGGTT	This paper	N/A
VEGFA_5' UTR -1038 Forward GGGGTACCTCGCGGAGGCTTGG GGCAGCCG	This paper	N/A
VEGFA_5' UTR -541 Reverse GAAGATCTCGCGACTGGTCAGC TGCGGGATC	This paper	N/A
VEGFA_5' UTR -540 Forward GGGGTACCCTGACGGACAGACA GACAGACAC	This paper	N/A
VEGFA_5' UTR -1 Reverse GAAGATCTGGTTTCGGAGGCCC GACCGGG	This paper	N/A
VEGFA_5' UTR AAA_ Forward GAGCACTGTCTGCGCTTTCCGC CGCCTCACCCG	This paper	N/A
VEGFA_5' UTR AAA_ Reverse CGGGTGAGGCGGCGGAAAGCGC AGACAGTGCTC	This paper	N/A
VEGFA_5' UTR AAAAA_Forward GCTGGAGCACTGTCTGCGCTTT TTGCCGCCTCACCCGTCCATG	This paper	N/A
VEGFA_5' UTR AAAAA_Reverse CATGGACGGGTGAGGCGGCAAA AAGCGCAGACAGTGCTCCAGC	This paper	N/A
hTRS qRT-PCR Forward GTAAGCCATGATGGTGA	This paper	N/A
hTRS qRT-PCR Reverse CTGCCTGTTTGCTGCGG	This paper	N/A
h4EHP qRT-PCR Forward CAGCACACAGAAAGATGGTGA	This paper	N/A
h4EHP qRT-PCR Reverse CTCCAGAACTGCTCCACAGAG	This paper	N/A
hVEGFA qRT-PCR Forward GCACCCATGGCAGAAGG	This paper	N/A
hVEGFA qRT-PCR Reverse CTCGATTGGATGGCAGTAGCT	This paper	N/A
hGAPDH qRT-PCR Forward AGCCACATCGCTCAGACAC	This paper	N/A
hGAPDH qRT-PCR Reverse GCCCAATACGACCAAATCC	This paper	N/A
hANG qRT-PCR Forward AGAAGCGGGTGAGAAACAA	This paper	N/A

hANG qRT-PCR Reverse TGTGGCTCGGTACTGGCATG	This paper	N/A
mTRS qRT-PCR Forward GCTCTAGATTATTCTGCCAGAA TGGAATCATGTTC	This paper	N/A
mTRS qRT-PCR Reverse ATAAGAATGCGGCCGCTAAAGG CAGAAAAAGATAGC	This paper	N/A
m4EHP qRT-PCR Forward GATGGAGGTCGAGCTGAGTTGA ATAAGGCAGAAAAAGA	This paper	N/A
m4EHP qRT-PCR Reverse TCTTTTTCTGCCTTATTCAACT CAGCTCGACCTCCATC	This paper	N/A
mVEGFA qRT-PCR Forward ATAGCGGATGGAAAACCCTGC	This paper	N/A
mVEGFA qRT-PCR Reverse TATCGCCTACCTTTTGGGACG	This paper	N/A
mGAPDH qRT-PCR Forward AGGCCGGTGCTGAGTATGTC	This paper	N/A
mGAPDH qRT-PCR Reverse TGCCTGCTTCACCACCTTCT	This paper	N/A
Morpholino: *trs* MO: GTGATTCTTCAAAACTGACCTC CCA	Gene-Tools	N/A
Morpholino: *4ehp* MO: GCGTGTGTGTAGGTTACCGAAG CA	Gene-Tools	N/A
Morpholino: standard control MO: CCTCTTACCTCAGTTACAATTT ATA	Gene-Tools	http://www.gene -tools.com/custo m_morpholinos_c ontrols_endmodifi cations#standardc ontrols

Discussion

Expansion in the complexity of molecular signaling during the evolution toward vertebrate lineage includes more intricate translation mechanisms and regulatory processes. Herein, the results uncovered a previously unidentified cap-dependent translation initiation mechanism that represents an evolutionary gain of function in vertebrates. This study demonstrate that the 4EHP-TRS-eIF4A complex would act similarly to the eIF4F complex, and is necessary for translation initiation of specific mRNAs in vertebrates.

While being essential for protein synthesis in all three domains of life, ARSs have cumulatively acquired new domains/regions to cope with the increasing demand of functional complexity required for higher organisms. Among these newly acquired additions, UNE regions that share no detectable sequence similarity with other structural modules of ARSs (17), and are expected to perform important unique functions (18). One particular example relevant to the emergence of vertebrates is the UNE-S region at the C-terminus of seryl-tRNA synthetase that is present in all vertebrates from fish to human (17). UNE-S containing a nuclear localization signal (NLS) engendered this enzyme the capability of working in nucleus for vascular development during establishment of the closed circulatory system of vertebrates (42).

In this study, the results discovered an unexpected role of TRS in regulating translation initiation in vertebrates. Among twenty human ARSs, TRS may have been selected for this function due to its structural features as following. First, it contains the eIF4E-binding motif, UNE-T at its N-terminal end. Second, it can select a specific set of mRNAs through the interaction with a unique anticodon-like

loop at 5'UTR. Third, its catalytic domain can recruit eIF4A and PABP. Considering that human TRS normally exists as a homodimer, it may also work as a dimer in the translation initiation complex. It would be interesting to see whether its dimeric interface would provide an additional structural contribution for TRS to serve as a scaffold for the translation initiation complex.

TRS-mediated RIP-seq analysis suggests that the 4EHP-TRS-eIF4A complex may regulate the translation initiation of mRNAs involved in biological processes that are unique to vertebrates and presumably important for processes of invertebrate-to-vertebrate transition including development of circulation, nervous and skeletal systems. This notion appears to be supported by the results of *in vitro* cell migration and vessel formation assays (Figures 10A-10I), and the formation of hindbrain central arteries (CtAs) in the developing zebrafish embryos, showing that 4EHP and TRS interaction-mediated translation is critical for normal embryonic angiogenesis and vasculogenesis (Figures 12A-12F). Vertebrates possess a more highly evolved and complex cardiovascular system compared to invertebrates. Mechanisms of vessel formation in the developing lung require embryonic cardiovascular development (43). Early endothelial cell differentiation followed by migration and tube formation is observed at embryonic day 10.5 during murine embryonic development, as is pulmonary vessel formation (44). In this regard, it is worth noting that this current results also showed the emergence of murine 4EHP and VEGF expression at embryonic day 10.5 (Figure 13). While TRS is being constitutively expressed, it can recruit timely expressed 4EHP and select a specific set of transcripts for enhanced translation. Although induced expression of 4EHP is crucial for the interaction

with TRS, it does not seem to be the sole determinant for the formation of their translation initiation complex since 4EHP does not form the similar complex with TRS in fly even though it is expressed (Figure 5D). Consequently, vertebrate-specific acquisition of UNE-T domain was additionally required to link these two factors for translational control.

This study reports the first molecular evidence showing that the functional directionality of the 4EHP-containing translation initiation complex would be determined by its interacting partner(s). For instance, while the complex of 4EHP with Bicoid or Grb10-interacting GYF protein 2 was shown to inhibit translation initiation (14-16), this study report here that its complex with TRS enhanced translation initiation of specific mRNAs. It would be interesting to see whether 4EHP would be involved in the formation of other translation regulatory complexes in distinct biological contexts. It was previously shown that methionyl-tRNA synthetase (MRS) can block translation initiation in response to DNA damage (45). In this case, GCN2 activated by DNA damage inactivates the methionine-charging capability of MRS to block nascent protein synthesis until the damaged DNAs is repaired. Combined together, ARSs appear to be equipped to control translation initiation in either direction via their catalytic and non-catalytic routes.

Materials and Methods

Cell culture

HEK293T and WI-26 cells were grown in DMEM (Hyclone) containing 10% fetal bovine serum (FBS, Hyclone) and antibiotics. Cell lines were cultured in 5% CO_2 at 37°C. CHO and THP1 cells were grown in RPMI (Hyclone) containing 10% FBS and antibiotics. THP1 cells were differentiated to the adherent macrophage-like state by treatment with 50 ng/ml of phorbol 12-myristate 13-acetate (Sigma) for 36 h. Adherent, differentiated cells were washed with cold PBS every 24 h for the next 3 days. The resultant cells were used as differentiated THP1 cells. Drosophila Schneider S2 cells were propagated at 28°C in Schneider's Drosophila medium (Life Technologies) supplemented with 10% FBS, 50 units/ml penicillin, and 50 μg/ml streptomycin. Human brain VSMCs were maintained in SMCM (ScienCell) and used between passages two and four. HUVECs were maintained in EGM-2 complete media (Lonza) and used between passages 5 and 9.

DNA cloning

Human eIF4E1, eIF4E2, eIF4A, and eIF4G were cloned into the pIRES-FLAG vector (47). Constructs for human eIF4E3 was purchased from Origene. The functional domains of human TRS were cloned into the pEBG-GST vector (Addgene). Human 4EHP, mouse 4EHP, zebrafish 4EHP, and drosophila 4EHP were cloned into the pcDNA3.1-HA vector (Invitrogen). Human TRS, mouse TRS, zebrafish TRS, and drosophila TRS were cloned into the pcDNA3.1/Myc-His A vector (Invitrogen). Human TRS, drosophila TRS, Human 4EHP, and drosophila 4EHP were cloned into the

pAc5.1/V5-His A vector (Invitrogen). Human TRS, AlaRS, and SRS were cloned into the pEXPR-IBA103 vector (IBA). Human TRS was cloned into the pEXPR-IBA105 vector (IBA). All luciferase constructs were generated by cloning the respective PCR fragment into the pGL2 luciferase reporter vector (Promega). The pRL *Renilla* luciferase vector (Promega) was co-transfected in all experiments and used for normalization of transfection efficiency. To produce the stable human 4EHP in complex with human TRS, the plasmid co-expressing two proteins was constructed using a two promoter vector system (48). In this construct, N-terminal extension domain of TRS and 4EHP (residues 45-234) were independently expressed under the control of the T7 promoter and the Tac promoter, respectively. Briefly, the gene encoding $4EHP_{45-234}$ was PCR-cloned into the pMBP-Parallel1 expression vector(49), which expresses tag-free N-terminal extension domain of human TRS. For isothermal titration calorimetry (ITC) experiment, the gene encoding N-terminal extension domain of human TRS was sub-cloned into the pET22b vector (Invitrogen) containing a C-terminal hexahistidine (His)-tag and the gene for 4EHP was sub-cloned into the pGST-Parallel1 expression vector (49). The sequences of the primers used are listed in Key Resources Table. All constructs were confirmed by DNA sequencing.

Antibodies and reagents

Antibodies were obtained from the following sources: HA, c-Myc, GFP, TRS, AlaRS, VEGF-A, and ANG1, as well as HRP-labeled anti-mouse and anti-rabbit secondary antibodies, were from Santa Cruz Biotechnology; antibodies to GST, eIF4A, and eIF4G1 were from Cell Signaling Technology; antibodies to alpha-tubulin and FLAG were from Sigma-Aldrich; antibody to 4EHP was from Genetex;

antibody to Strep was from IBA; antibody to eIF4E was from BD Biosciences; antibodies to Alexa Fluor 488 Phalloidin, Alexa 647, Alexa 594, and V5 were from Thermo Fisher. Transfection was performed using Lipofectamine 2000 (Invitrogen), Fugene HD (Roche) and TurboFect (Thermo Fisher). Strep-Tactin-coated magnetic beads (Magstrep type3 XT beads) were purchased from IBA.

Preparation of cell lysates and immunoprecipitation

Cells were dissolved in lysis buffer containing 1% Triton X-100, 50 mM HEPES (pH 7.4), 150 mM NaCl, 2 mM EDTA, 10 mM pyrophosphate, 10 mM glycerophosphate, and protease inhibitor cocktail (Calbiochem), and lysates were centrifuged at 13,000 rpm for 15 min. Then, 20 mg of the extracted proteins was fractionated by SDS-PAGE. For Strep-tagged protein precipitation, cells were lysed and Magstrep type3 XT beads were added and used according to the manufacturer's instructions. For immunoprecipitation, cells were lysed and primary antibodies were added and incubated with agitation for 4 h at 4°C. A 50% slurry of protein agarose G-Sepharose was then added, and the incubation continued for an additional 4 h. After washing three times with ice-cold lysis buffer, precipitates were dissolved in SDS sample buffer and separated by SDS-PAGE.

Bimolecular fluorescence complementation (BiFC) assay

TRS and AlaRS were cloned into pBiFC-VN173 (FLAG tag). 4EHP and eIF4E were cloned into pBiFC-VC155 (HA tag). CHO cells were co-transfected with pBiFC-VN173-TRS or pBiFC-VN173-AlaRS together with pBiFC-VC155-4EHP or pBiFC-VC155-eIF4E. These cells were fixed with 100% methanol for 7 min at room temperature and incubated with blocking solution (3% CAS) for 15 min at room

temperature. After blocking, cells were stained with HA, Alexa 647, FLAG, and Alexa 594 for 1 h at room temperature, respectively. DAPI was used for nuclear staining. Cells were washed three times with PBS every step. After mounting, the TRS and 4EHP interaction was observed by fluorescence and confocal microscopy (Nikon, A1Rsi).

Protein expression and purification

E. coli BL21 (DE3) cells harboring co-expression plasmids were grown in LB medium containing ampicillin at 37°C until the optical density of 600 nm reached between 0.4 and 0.6. Thereafter, the temperature of culture media was decreased to 18°C and the expression of target proteins was induced by the addition of 0.5 mM IPTG for 20 h. Recombinant proteins were purified using Ni-NTA affinity chromatography and then treated with rTEV protease to cleave the MBP-hexahistidine-tag from 4EHP (residues 45-234). Protein solution was then applied to the Superdex75, 16/60 column (GE Healthcare) equilibrated at 4°C with 50 mM Tris-HCl (pH 8.0), 300 mM NaCl for size-exclusion chromatography. The fractions containing the 4EHP (45-234) in complex with N-terminal extension domain of TRS were collected and carried out additional Ni-NTA affinity chromatography for further purification.

In vitro TRS- and 4EHP-binding assay

Plasmids expressing His-tagged *Drosophila* TRS (residues 1 - 50) and His-tagged human TRS (residues 1 - 74) were transformed into *E. coli* BL21(DE3) cells. GST-fused *Drosophila* 4EHP and GST-fused human 4EHP were transformed into *E. coli* Rosetta-gami (DE3) pLysS and BLR, respectively. Protein expression was induced by

59

treatment with 0.5 mM IPTG at 18°C for 20 h. Harvested cells were resuspended in Buffer A (50 mM Tris-HCl, pH 8.0, 300 mM NaCl) and lysed by sonication on ice. Cell lysates were centrifuged at 25,000 ´ g at 4°C for 1 h. Supernatants containing His-tagged TRS and GST-fused 4EHP were loaded onto a Ni-NTA agarose column, washed extensively with Buffer A, and eluted with 250 mM imidazole. All eluted proteins were analyzed by SDS-PAGE, followed by staining with Coomassie Brilliant Blue.

Isothermal titration calorimetry (ITC)

The 4EHP (45-234)was purified and prepared as previously description (22). The gene encoding TRS (1-74) was expressed as C-terminal His-tagged proteins under the same conditions as the cells containing co-expression plasmids and the recombinant TRS (1-74) was purified as described for the complex proteins. The proteins were degassed by vacuum aspiration for 15 min before loading, and titration experiment was carried out at 25°C with a VP-ITC titration calorimeter (MicroCal Inc. Northampton, MA). TRS (1-74) was placed in the syringe (0.6 mM) and titrated against the 4EHP (45-234) in the reaction cell (0.035 mM). Raw data were fitted to a single binding site model by using the Origin program (version 7.0), which was supplied with the instrument.

Crystallization and structure determination

Even though the crystals of 4EHP (45-234) in complex with TRS (1-74) were obtained using *in situ* proteolysis method and diffracted well, the determination of protein structure was failed due to phasing problem. Therefore, several truncated variants of N-terminal extension domain of TRS in complex with 4EHP (45-234) were purified as

described above and crystallized using the sitting drop vapor-diffusion method at 21°C. The initial crystal hits were obtained with 4EHP (45-234) -TRS (30-74) complex. The crystals of this complex for X-ray diffraction were optimized in the following conditions: 20 % PEG8000 and 0.1M CHES (pH9.5). The best crystals appeared within 3days. For diffraction experiment, the complex crystals were transferred to acryoprotectant solution consisting of 20 % PEG8000, 0.1M CHES (pH9.5) and 20 % (v/v) glycerol, and then mounted immediately in a –173°C nitrogen gas stream. The diffraction data for the complex crystals were collected at 1.9 Å resolution and processed with the HKL2000 package (50). The structure of protein complex was solved by molecular replacement using the program Phaser-MR of Phenix (51) with the structure of 4EHP (PDB 2JGB) as the search model. The structure was revised by using the COOT program (52) and refined by using Phenix.refine (51).

Mutation of TRS and 4EHP

Point mutations in *TRS* and *4EHP* were generated via site-directed mutagenesis using a QuickChange Kit (Agilent) following the manufacturer's instructions, and mutants were confirmed by DNA sequencing. The sequences of the primers used are listed in Key Resources Table.

Aminoacylation assay

The aminoacylation assay was carried out in buffer containing 4 mM DTT, 50 mM HEPES-KOH (pH 7.6), 20 mM KCl, 10 mM $MgCl_2$, 5 mM ATP, 2 mg/ml yeast tRNA (Roche), various concentrations of [3H]Thr (American Radiolabeled Chemicals), and 100nM TRS. Reactions were initiated with enzyme and conducted in a 37°C heat

block. Aliquots (10 ml) were taken at different time points and quenched on Whatman filter pads that were presoaked with 5% trichloroacetic acid (TCA). Pads were washed three times for 10 min each time with cold 5% TCA, and once with cold 100% ethanol. Washed pads were then dried, and radioactivity was quantified using a scintillation counter (Beckman Coulter).

Cap-binding assay

Cells were washed with PBS and lysed in lysis buffer (20 mM Tris-HCl, pH 7.5, 100 mM NaCl, 25 mM $MgCl_2$, 0.5 % NP40, and protease inhibitor cocktail). Extracts were clarified by centrifugation at 10,000´ g for 10 min at 4℃. Supernatants were pre-cleared with 30 µl of agarose beads (Sigma) for 1 h at 4℃, beads were removed by centrifugation at 500 ´ g for 1 min, and supernatants were incubated with 50 µl of 7-methyl GTP-agarose beads (Jena Bioscience) for 2 h at 4℃. Pelleted beads were washed four times with 0.5 ml of lysis buffer, resuspended in sample buffer, and boiled for 5 min. 7-methyl GTP-bound proteins, as well as 5% of the initial sample taken just before the 7-methyl GTP beads were added, were subjected to SDS-PAGE.

RNA interference

Cells were transfected with duplex siRNA using the Lipofectamine 2000 transfection reagent (Invitrogen) according to the manufacturer's instructions. ON-TARGETplus SMARTpool siRNAs against TRS, AlaRS, 4EHP, and eIF4E were purchased from GE Healthcare Dharmacon. Stealth RNAi siRNAs against eIF4G was purchased from Thermo Fisher. The sequences of siRNAs used in this study are provided in Key Resources Table. A non-targeting siRNA was used

as a control. Cells were incubated with the siRNA for 36-72 h.

Puromycin incorporation assay (SUnSET assay)

SUnSET was performed as previously described (34). Briefly, cells were incubated with 1 μM puromycin (Thermo Fisher) for 30 min followed by washing with ice cold PBS and lysing with lysis buffer. Cell lysates were loaded onto SDS-PAGE and performed western blots with mouse anti-puromycin monoclonal antibody (Millipore) and normalized against Ponceau S staining (INtRON).

RNA-immunoprecipitation and sequencing (RIP-Seq)

RNA immunoprecipitation was performed according to the manufacturer's protocol using a Dynabeads Co-Immunoprecipitation Kit (Thermo Fisher). In brief, lysed HEK293T cells (5 ´ 10^8 cells per sample) were incubated with rabbit anti-TRS, rabbit IgG, or anti-AlaRS antibody-coupled Dynabeads for 45 min at 4°C. After multiple washes, RNA was extracted from the beads by vortexing for 30 s with PCI buffer (phenol:chloroform:isoamyl alcohol, pH 4.5) and centrifuged at 16,000 ´ g for 2 min. The upper phase was transferred to a fresh tube, and RNA was precipitated by adding 20 mg/ml glycogen (Invitrogen), 0.1 volume of 3 M sodium acetate (pH 5.5), and 2.5 volume of 100% ethanol. The mixtures were incubated at -20°C for 1 h and centrifuged at 16,000 ´ g for 5 min. The final RNA pellets were air-dried and re-suspended in RNase-free water for sequencing. The sequencing library was prepared using the TruSeq RNA sample preparation kit v2 (Illumina) as previously reported (53). In brief, mRNA derived from total RNA using poly-T oligo-attached magnetic beads was fragmented and converted into cDNA, adapters were ligated, and fragments were amplified by PCR.

Paired-end sequencing (2 ´ 10) was performed using a Hiseq-2000 system (Illumina). Reference genome sequence data from *Homo sapiens* were obtained from the University of California Santa Cruz Genome Browser Gateway (assembly ID: hg19). The reference genome index was built using SAMtools (v. 0.1.19) and the Bowtie2-build component of Bowtie2 (v. 2.1.0). Reads were mapped to the reference genome using Tophat2 (v. 2.0). The number of reads per kilobase per million mapped reads (rpkm) for each gene of 46,895 RefSeq (UCSC hg19) gene models was calculated using Cufflinks (v. 2.2.1). Heat maps were constructed using Mev (v. 4.9.0). Statistical analyses and graph construction were performed using R (v. 3.1.0) and PYTHON (v. 2.7.6). For functional annotation analysis, DAVID (database for annotation, visualization and integrated discovery; http://david.abcc.ncifcrf.gov) was used (39). The enriched gene set was obtained from Ensemble Biomart (http://www.biomart.org) (54).

RNA secondary structure prediction

The sequence from human VEGF 5′ UTR (GeneBank accession no. NM_001025366) was submitted to RNA fold web server (55) (http://rna.tbi.univie.ac.at/cgi-bin/RNAfold.cgi) for secondary structure prediction.

Luciferase reporter assay

Luciferase assays were performed using the Luciferase Assay System & *Renilla* Luciferase assay System (Promega) according to the manufacturer's instructions. Briefly, HEK293T cells were transfected with the luciferase reporter plasmid pGL2 combined with the VEGF 5′ UTR sequence. At 24 h after transfection, cells were lysed and reporter activity was analyzed with the Luciferase Assay System &

Renilla Luciferase assay System (Promega).

Real-time RT-PCR

Total RNA was extracted from cells using the RNeasy RNA extraction Mini-Kit (QIAGEN). Purified RNA was treated with RNase-free DNase at 37°C for 30 min. Quantitative PCR was performed using gene-specific primer sets (Bioneer, Korea) and SYBR Green Supermix (Biorad). Real-time PCR was carried out in a LightCycler 96 (Roche Diagnostics, Germany) according to the manufacturer's instructions. Data were normalized against *glyceraldehyde-3-phosphate dehydrogenase* expression. Relative expression was calculated using the DDCT method. The sequences of the primers used are listed in Key Resources Table.

Enzyme-linked immunosorbent assay (ELISA)

The angiogenic cytokine concentration in cell culture supernatants was measured by ELISA according to the manufacturer's instructions using the following kits: VEGF, angiogenin (R&D Systems).

Secretion assay

For cell culture media samples, cells were incubated for 16 h in serum-free medium. After centrifugation for 5 min at 200 ´ g to remove cells, the supernatant was concentrated 10-fold using an Amicon Ultra-4 centrifugal filter unit (Millipore).

In vitro tube formation assay

HUVECs were cultured until 95-100% confluent and seeded in 48-well plates coated with Matrigel Basement Membrane Matrix GFR (BD Biosciences). Cells were incubated at 37 °C in EGM-2 media

with 2% FBS and various media for 4 to 8 h. Cells were fixed with 4% paraformaldehyde, stained with Alexa Fluor 488 phalloidin (Life technology), and imaged by fluorescence microscopy. Tube structures were quantified using ImageJ software (NIH).

Cell migration assay

Cell migration was determined using 24-well Transwell chambers with a polycarbonate membrane (8.0 μm pore size; Corning). HUVECs were suspended in EBM2 basal medium and added to the top chamber at a density of 1 ´ 10^4 cells/well. To determine the effect of siTRS and si4EHP, various conditioned media were placed in the bottom chamber, and cells were allowed to migrate for 6 h at 37℃, fixed with 70% methanol in PBS for 30 min, washed with PBS three times, stained with hematoxylin (Sigma-Aldrich) for 10 min, and washed with distilled water. Non-migrating cells were removed from the top face of the membrane with a cotton swab, and membranes were excised from the chamber and mounted with Gel Mount (Biomeda). Migrating cells attached to the bottom face of the membrane were counted using three randomly selected views in high-power fields (20).

Zebrafish husbandry and embryo fixation

The endothelial-specific transgenic line *Tg*(*kdrl:EGFP*) and WT AB line were maintained at the zebrafish facility in the Korea Research Institute of Bioscience & Biotechnology under a 14:10 h light:dark cycle. Embryos were collected and raised at 28.5 ℃, treated with 1-phenyl 2-thiourea (PTU, Sigma) to prevent pigmentation, and fixed at 52 h post-fertilization (hpf) with 4 % paraformaldehyde in PBS and staining solution to preserve EGFP fluorescence after fixation.

Fixed zebrafish larvae were embedded on 1.3% low melting point agarose (Promega), and confocal images were taken using an Olympus FV1000 confocal microscope. Z-projected images were used to measure the length and branching points of vessels using ImageJ software.

Morpholinos and mRNA injection into zebrafish embryos

Splicing-blocking morpholinos (MOs) for *trs* (*trs*-MO, 5'-GTG ATT CTT CAA AAC TGA CCT CCC A-3') and *4ehp* (*4ehp*-MO, 5'-GCG TGT GTG TAG GTT ACC GAA GCA A-3') were ordered from GeneTools (http://www.gene-tools.com/), targeting exon4 and exon3, respectively. *trs*-MO (500 mM) and *4ehp*-MO (200 mM) were injected to transiently knockdown TRS and 4EHP expression without causing gross morphological defects to developing larvae. A standard control MO (5'-CCT CTT ACC TCA GTT ACA ATT TAT A-3') was used as a negative control. Functional mRNAs were *in vitro* synthesized using the mMESSAGE mMACHINE SP6 Transcription Kit (Ambion, AM1340) according to the manual, with *Not*I-linearized plasmid containing an appropriate full-length cDNA (WT TRS, I55D mutant TRS, WT 4EHP, or mCherry as a negative control) in the pCS2+ vector. Overexpression experiments were carried out using 0.2 ng of each mRNA, but 0.4 ng was used in the case of the control mRNA alone. In rescue experiments, 0.4 ng of each mRNA was co-injected with *trs*-MO or *4ehp*-MO. All injections were carried out when fertilized eggs were at the 1-2 cell stage.

Preparation of total protein from mouse tissues

Embryos were collected at postcoital days from 8.5 to 12.5 of C57BL/6 mouse. For detection of proteins, embryos were placed in a

buffer containing 1% Triton X-100, 50 mM HEPES (pH 7.4), 150 mM NaCl, 2 mM EDTA, 10 mM pyrophosphate, 10 mM glycerophosphate, and protease inhibitor cocktail for homogenization. Samples were homogenized at 4°C for 30 s, incubated on ice for 30 s, and then homogenized again for 30 s using a homogenizer microtube (COSMOBIO). Lysates were centrifuged at 13,000 rpm for 15 min at 4°C, and supernatants were collected.

Statistical analyses

Statistical analyses were performed using Prism 6 (GraphPad). Bar graphs were plotted as means ± SEM and statistical significance was denoted as follows: Not significant, $p \geq 0.05$, $^*p < 0.05$; $^{**}p < 0.01$; $^{***}p < 0.001$, $****$, $p < 0.0001$.

References

1. Jackson RJ, Hellen CU, Pestova TV. The mechanism of eukaryotic translation initiation and principles of its regulation. Nat Rev Mol Cell Biol. 2010;**11**:113-27.

2. Schwanhausser B, Busse D, Li N, Dittmar G, Schuchhardt J, Wolf J, et al. Global quantification of mammalian gene expression control. Nature. 2011;**473**:337-42.

3. Richter JD, Coller J. Pausing on Polyribosomes: Make Way for Elongation in Translational Control. Cell. 2015;**163**:292-300.

4. Gingras AC, Raught B, Sonenberg N. eIF4 initiation factors: effectors of mRNA recruitment to ribosomes and regulators of translation. Annu Rev Biochem. 1999;**68**:913-63.

5. Sonenberg N, Hinnebusch AG. Regulation of translation initiation in eukaryotes: mechanisms and biological targets. Cell. 2009;**136**:731-45.

6. Hellen CU, Sarnow P. Internal ribosome entry sites in eukaryotic mRNA molecules. Genes Dev. 2001;**15**:1593-612.

7. Braunstein S, Karpisheva K, Pola C, Goldberg J, Hochman T, Yee H, et al. A hypoxia-controlled cap-dependent to cap-independent translation switch in breast cancer. Mol Cell. 2007;**28**:501-12.

8. Brugarolas J, Lei K, Hurley RL, Manning BD, Reiling JH, Hafen E, et al. Regulation of mTOR function in response to hypoxia by REDD1 and the TSC1/TSC2 tumor suppressor complex. Genes Dev. 2004;**18**:2893-904.

9. Koritzinsky M, Magagnin MG, van den Beucken T, Seigneuric R, Savelkouls K, Dostie J, et al. Gene expression during acute and prolonged hypoxia is regulated by distinct mechanisms of translational control. EMBO J. 2006;**25**:1114-25.

10. Liu L, Cash TP, Jones RG, Keith B, Thompson CB, Simon MC.

Hypoxia-induced energy stress regulates mRNA translation and cell growth. Mol Cell. 2006;**21**:521-31.

11. Uniacke J, Holterman CE, Lachance G, Franovic A, Jacob MD, Fabian MR, et al. An oxygen-regulated switch in the protein synthesis machinery. Nature. 2012;**486**:126-9.

12. Hernandez G, Altmann M, Sierra JM, Urlaub H, Diez del Corral R, Schwartz P, et al. Functional analysis of seven genes encoding eight translation initiation factor 4E (eIF4E) isoforms in Drosophila. Mech Dev. 2005;**122**:529-43.

13. Rom E, Kim HC, Gingras AC, Marcotrigiano J, Favre D, Olsen H, et al. Cloning and characterization of 4EHP, a novel mammalian eIF4E-related cap-binding protein. J Biol Chem. 1998;**273**:13104-9.

14. Cho PF, Poulin F, Cho-Park YA, Cho-Park IB, Chicoine JD, Lasko P, et al. A new paradigm for translational control: inhibition via 5′-3′ mRNA tethering by Bicoid and the eIF4E cognate 4EHP. Cell. 2005;**121**:411-23.

15. Cho PF, Gamberi C, Cho-Park YA, Cho-Park IB, Lasko P, Sonenberg N. Cap-dependent translational inhibition establishes two opposing morphogen gradients in Drosophila embryos. Curr Biol. 2006;**16**:2035-41.

16. Morita M, Ler LW, Fabian MR, Siddiqui N, Mullin M, Henderson VC, et al. A novel 4EHP-GIGYF2 translational repressor complex is essential for mammalian development. Mol Cell Biol. 2012;**32**:3585-93.

17. Guo M, Yang XL, Schimmel P. New functions of aminoacyl-tRNA synthetases beyond translation. Nat Rev Mol Cell Biol. 2010;**11**:668-74.

18. Guo M, Yang XL. Architecture and metamorphosis. Top Curr Chem. 2014;**344**:89-118.

19. Guo M, Schimmel P, Yang XL. Functional expansion of human

tRNA synthetases achieved by structural inventions. FEBS Lett. 2010;**584**:434-42.

20. Torres-Larios A, Dock-Bregeon AC, Romby P, Rees B, Sankaranarayanan R, Caillet J, et al. Structural basis of translational control by Escherichia coli threonyl tRNA synthetase. Nat Struct Biol. 2002;**9**:343-7.

21. Dong A, Xu X, Edwards AM, Midwest Center for Structural G, Structural Genomics C, Chang C, et al. In situ proteolysis for protein crystallization and structure determination. Nat Methods. 2007;**4**:1019-21.

22. Rosettani P, Knapp S, Vismara MG, Rusconi L, Cameron AD. Structures of the human eIF4E homologous protein, h4EHP, in its m7GTP-bound and unliganded forms. J Mol Biol. 2007;**368**:691-705.

23. Peter D, Igreja C, Weber R, Wohlbold L, Weiler C, Ebertsch L, et al. Molecular architecture of 4E-BP translational inhibitors bound to eIF4E. Mol Cell. 2015;**57**:1074-87.

24. Gruner S, Peter D, Weber R, Wohlbold L, Chung MY, Weichenrieder O, et al. The Structures of eIF4E-eIF4G Complexes Reveal an Extended Interface to Regulate Translation Initiation. Mol Cell. 2016;**64**:467-79.

25. Wolf YI, Aravind L, Grishin NV, Koonin EV. Evolution of aminoacyl-tRNA synthetases--analysis of unique domain architectures and phylogenetic trees reveals a complex history of horizontal gene transfer events. Genome Res. 1999;**9**:689-710.

26. Francklyn C, Musier-Forsyth K, Martinis SA. Aminoacyl-tRNA synthetases in biology and disease: new evidence for structural and functional diversity in an ancient family of enzymes. RNA. 1997;**3**:954-60.

27. Mader S, Lee H, Pause A, Sonenberg N. The translation initiation

factor eIF-4E binds to a common motif shared by the translation factor eIF-4 gamma and the translational repressors 4E-binding proteins. Mol Cell Biol. 1995;**15**:4990-7.

28. Marcotrigiano J, Gingras AC, Sonenberg N, Burley SK. Cap-dependent translation initiation in eukaryotes is regulated by a molecular mimic of eIF4G. Mol Cell. 1999;**3**:707-16.

29. Hernandez G, Vazquez-Pianzola P. Functional diversity of the eukaryotic translation initiation factors belonging to eIF4 families. Mech Dev. 2005;**122**:865-76.

30. Zuberek J, Kubacka D, Jablonowska A, Jemielity J, Stepinski J, Sonenberg N, et al. Weak binding affinity of human 4EHP for mRNA cap analogs. RNA. 2007;**13**:691-7.

31. Joshi B, Cameron A, Jagus R. Characterization of mammalian eIF4E-family members. Eur J Biochem. 2004;**271**:2189-203.

32. Tarun SZ, Jr., Sachs AB. Association of the yeast poly(A) tail binding protein with translation initiation factor eIF-4G. EMBO J. 1996;**15**:7168-77.

33. Tarun SZ, Jr., Wells SE, Deardorff JA, Sachs AB. Translation initiation factor eIF4G mediates in vitro poly(A) tail-dependent translation. Proc Natl Acad Sci U S A. 1997;**94**:9046-51.

34. Schmidt EK, Clavarino G, Ceppi M, Pierre P. SUnSET, a nonradioactive method to monitor protein synthesis. Nat Methods. 2009;**6**:275-7.

35. Coldwell MJ, Morley SJ. Specific isoforms of translation initiation factor 4GI show differences in translational activity. Mol Cell Biol. 2006;**26**:8448-60.

36. Yanagiya A, Suyama E, Adachi H, Svitkin YV, Aza-Blanc P, Imataka H, et al. Translational homeostasis via the mRNA cap-binding protein, eIF4E. Mol Cell. 2012;**46**:847-58.

37. Gallie DR. The cap and poly(A) tail function synergistically to regulate mRNA translational efficiency. Genes Dev. 1991;**5**:2108-16.

38. Michel YM, Poncet D, Piron M, Kean KM, Borman AM. Cap-Poly(A) synergy in mammalian cell-free extracts. Investigation of the requirements for poly(A)-mediated stimulation of translation initiation. J Biol Chem. 2000;**275**:32268-76.

39. Huang da W, Sherman BT, Lempicki RA. Systematic and integrative analysis of large gene lists using DAVID bioinformatics resources. Nat Protoc. 2009;**4**:44-57.

40. Gruber AR, Bernhart SH, Hofacker IL, Washietl S. Strategies for measuring evolutionary conservation of RNA secondary structures. BMC Bioinformatics. 2008;**9**:122.

41. Williams TF, Mirando AC, Wilkinson B, Francklyn CS, Lounsbury KM. Secreted Threonyl-tRNA synthetase stimulates endothelial cell migration and angiogenesis. Sci Rep. 2013;**3**:1317.

42. Xu X, Shi Y, Zhang HM, Swindell EC, Marshall AG, Guo M, et al. Unique domain appended to vertebrate tRNA synthetase is essential for vascular development. Nat Commun. 2012;**3**:681.

43. Baldwin HS. Early embryonic vascular development. Cardiovasc Res. 1996;**31**:E34-45.

44. Schachtner SK, Wang Y, Scott Baldwin H. Qualitative and quantitative analysis of embryonic pulmonary vessel formation. Am J Respir Cell Mol Biol. 2000;**22**:157-65.

45. Kwon NH, Kang T, Lee JY, Kim HH, Kim HR, Hong J, et al. Dual role of methionyl-tRNA synthetase in the regulation of translation and tumor suppressor activity of aminoacyl-tRNA synthetase-interacting multifunctional protein-3. Proc Natl Acad Sci U S A. 2011;**108**:19635-40.

46. Sankaranarayanan R, Dock-Bregeon AC, Romby P, Caillet J,

Springer M, Rees B, et al. The structure of threonyl-tRNA synthetase-tRNA(Thr) complex enlightens its repressor activity and reveals an essential zinc ion in the active site. Cell. 1999;**97**:371-81.

47. Gack MU, Shin YC, Joo CH, Urano T, Liang C, Sun L, et al. TRIM25 RING-finger E3 ubiquitin ligase is essential for RIG-I-mediated antiviral activity. Nature. 2007;**446**:916-20.

48. Kim KJ, Kim HE, Lee KH, Han W, Yi MJ, Jeong J, et al. Two-promoter vector is highly efficient for overproduction of protein complexes. Protein Sci. 2004;**13**:1698-703.

49. Sheffield P, Garrard S, Derewenda Z. Overcoming expression and purification problems of RhoGDI using a family of "parallel" expression vectors. Protein Expr Purif. 1999;**15**:34-9.

50. Otwinowski Z, Minor W. Processing of X-ray diffraction data collected in oscillation mode. Methods Enzymol. 1997;**276**:307-26.

51. Adams PD, Afonine PV, Bunkoczi G, Chen VB, Davis IW, Echols N, et al. PHENIX: a comprehensive Python-based system for macromolecular structure solution. Acta Crystallogr D Biol Crystallogr. 2010;**66**:213-21.

52. Emsley P, Cowtan K. Coot: model-building tools for molecular graphics. Acta Crystallogr D Biol Crystallogr. 2004;**60**:2126-32.

53. Kim SK, Kim SY, Kim JH, Roh SA, Cho DH, Kim YS, et al. A nineteen gene-based risk score classifier predicts prognosis of colorectal cancer patients. Mol Oncol. 2014;**8**:1653-66.

54. Smedley D, Haider S, Durinck S, Pandini L, Provero P, Allen J, et al. The BioMart community portal: an innovative alternative to large, centralized data repositories. Nucleic Acids Res. 2015;**43**:W589-98.

55. Gruber AR, Lorenz R, Bernhart SH, Neubock R, Hofacker IL. The Vienna RNA websuite. Nucleic Acids Res. 2008;**36**:W70-4.

Chapter II.

Inhibition of MUC1 biosynthesis via threonyl-tRNA synthetase suppresses pancreatic cancer cell migration

Running title: Catalytic activity for mucin biosynthesis

Keywords: Mucin1, Threonine-rich protein, Pancreatic cancer, Threonyl-tRNA synthetase, Cancer cell migration

Abbreviation

MUC1 : Mucin 1

MUC-CT : cytoplastic tail of MUC1

TRS : Threonyl-tRNA synthetase

ARS : Aminoacyl-tRNA synthetase

TCGA : The cancer genome atlas

CHX : Cycloheximide

SUnSET : Surface sensing of translation

Dox : Doxycyclin

BN : Borrelidin

ThrAMS : 5'-O-(N-(L-threonyl)-sulfamoyl) adenosine

TMA : Tissue microarray

Abstract

Mucin1 (MUC1), a heterodimeric oncoprotein, containing tandem repeat structure with a high proportion of threonine, is aberrantly overexpressed in many human cancers including pancreatic cancer. Since the survival of pancreatic cancer patients has remained low for several decades, novel therapeutic approaches are highly needed. Intestinal mucin has been known to be affected by dietary threonine supply since *de novo* synthesis of mucin proteins is sensitive to luminal threonine concentration. However, it is unknown whether biosynthesis of MUC1 is regulated by threonine in human cancers. In this study, data provided suggests that threonine starvation reduces the level of MUC1 and inhibits the migration of MUC1-expressing pancreatic cancer cells. Interestingly, knockdown of threonyl-tRNA synthetase (TRS), an enzyme that catalyzes ligation of threonine to its cognate tRNA, also suppresses MUC1 levels but not mRNA level. The inhibitors of TRS decrease the level of MUC1 protein and prohibit the migration of MUC1-expressing pancreatic cancer cells. In addition, a positive correlation between TRS and MUC1 levels is observed in human pancreatic cancer cells. Concurrent with these results, the bioinformatics data indicate that co-expression of both TRS and MUC1 is correlated with poor survival of pancreatic cancer patients. Taken together, these findings suggest the role of TRS in controlling the MUC1-mediated cancer cell migration and provide novel insight into targeting TRS as a new way to pancreatic cancer treatment.

Introduction

Pancreatic cancer is one of the most aggressive human cancers. The lack of early diagnoses and effective treatment strategies are critical factors that can lead to rapid death and low survival rates of pancreatic cancer patients (1). Even after surgically resected with a curative intent, the prognosis is very poor due to the high rate of metastasis (2). Hence, new strategies to find a novel therapeutic target are required to improve the treatment of pancreatic cancer (3).

MUC1, a member of the mucin family and a heterogeneous glycoprotein, is normally expressed at the apical surface of polarized epithelial cells of the mammary gland, stomach, duodenum, pancreas, uterus, prostate, and lungs (4). In malignancy, MUC1 is overexpressed and repositioned over the entire cell membrane of carcinoma cells and contributes to neoplastic transformation, tumor survival, angiogenesis, and metastasis (5). Additionally, the cytoplasmic tail of MUC1 (MUC1-CT) mediates intracellular signaling functions associated with cancer cell survival and metastasis (6). Aberrant overexpression of MUC1 is found in most human carcinomas including pancreatic cancer (7) and often used as a diagnostic marker for metastatic progression (8).

Mucins have a central backbone rich in threonine, proline, and serine residues that account for 20 to 55% of the total amino acid composition (9), with threonine alone constituting 28-35% of the total amino acids (10). In comparison with other essential amino acids, threonine is particularly important for maintenance of the gut and a large proportion of threonine is retained in the intestines of piglet and

humans (11, 12). Although previous reports show that mucin synthesis is sensitive to dietary threonine supply in the intestines of rats, pigs, piglets, and mice (13–17), it is unknown whether mucins are affected by threonine in human cancer cells.

In this study, it is discovered that the levels of MUC1 are affected by threonine in human pancreatic cancer cells. The data presented has identified that the protein level of MUC1 is also affected by threonyl–tRNA synthetase (TRS), which is one of the aminoacyl–tRNA synthetases (ARSs), an essential enzyme transferring threonine to cognate tRNA for protein synthesis (18). In addition, it is demonstrated that TRS affects the migration of pancreatic cancer cells through MUC1 biosynthesis. Moreover, it appears that expression of both TRS and MUC1 was positively correlated in pancreatic cancer cells, as well as associated with overall survival in the pancreatic cancer patients of the cancer genome atlas (TCGA) dataset.

Results

Threonine deprivation reduces MUC1 levels in pancreatic cancer cells

Since previous reports have shown that *de novo* synthesis of mucin was sensitive to threonine concentration (13-17), it is hypothesized that MUC1 would be affected by threonine in pancreatic cancer cells. Thus, it is examined whether MUC1 has a higher sensitivity threonine levels compared to other amino acids in the media. The removal of threonine (Thr-), but not phenylalanine (Phe-), valine (Val-) or tryptophan (Trp-) significantly reduced MUC1 and MUC1-CT levels (Figure 1a). However, no changes in MUC1 mRNA were observed in Panc 10.05 cells in which threonine was deprived (Figure 1b). Next, the time-dependent change of MUC1 levels after deprivation of threonine was investigated. When Panc 10.05 cells were incubated in threonine-free media, cellular levels of MUC1 and MUC1-CT were reduced in a time-dependent manner (Figure 1c) but mRNA levels of MUC1 were not changed under the same conditions (Figure 1d). To examine whether threonine depletion affects global translation or the level of MUC1, a $[^{35}S]$-Met incorporation assay was performed during threoine deprivation. Threonine deprivation had no effect on global protein synthesis in a time dependent manner, however significant inhibition of MUC1 levels was observed under the same conditions. Cycloheximide (CHX) (19), known as a protein translation inhibitor, completely blocked de novo protein synthesis. After withdrawal of threonine for 2 hrs, the threonine was added for 1 hr (Thr-/+) or 2 hrs (Thr-/++) to Panc 10.05 cells, and the result was restoration of the MUC1 and MUC1-CT level, further supporting

the effect of threonine to MUC1 (Figure 1e). In the course of these experiments, MUC1 protein levels were rapidly reduced in the absence of threonine. To further address this issue, MUC1 protein stability was measured after blocking *de novo* protein synthesis with CHX, and it was discovered that the half-life of MUC1, as well as MUC1-CT is shorter than 1.5 hrs (Figure 1f). These results suggest that MUC1 would need active biosynthesis to maintain its steady-state cellular level. In addition, the dependence of MUC1 on threonine in other pancreatic cancer cells was examined. The results showed a decrease in protein levels of MUC1 and MUC1-CT during the starvation of threonine in AsPC-1 and BxPC-3 cells (Figure 1g). Taken together, cancer-associated overexpression of MUC1 would demand the supply of threonine.

Threonine deprivation suppresses pancreatic cancer cell migration

It is known that MUC1 contributes to cancer cell migration (20-22). To verify the effect of threonine in MUC1-expressing pancreatic cancer cells, experiments that assessed the migration of pancreatic cancer cells following starvation of amino acids were performed. While migration of Panc 10.05 cells was significantly diminished by starvation of total amino acids, threonine displayed the highest sensitivity among single amino acid depletion (Figure 2a and b). In this experimental condition, cell growth was little affected (Figure 2c). Migration of other MUC1-expressing pancreatic cancer cells, AsPC-1 (Figure 2d) and BxPC-3 (Figure 2e) was also reduced in the absence of threonine. To evaluate whether migration by threonine deprivation is dependent on MUC1 level, Panc 10.05 cells were transfected with

siMUC1, and incubated in threonine-free media. The protein levels of MUC1 and MUC1CT were decreased by threonine deprivation or siMUC1 treatment. Knockdown of MUC1 decreased migration of Panc 10.05 cells and showed little effect on migration in the absence of threonine, indicating threonine-mediated decrease of migration is dependent on MUC1. Taken together, these results demonstrated that threonine deprivation suppresses the migration of pancreatic cancer cells expressing MUC1.

TRS regulates MUC1 biosynthesis

Since TRS catalyzes the ligation of threonine to its substrate tRNA for incorporation into nascently synthesized proteins, the inhibition of TRS catalytic activity or its expression can reduce MUC1 biosynthesis. To assess this possibility, TRS expression was suppressed using its specific siRNAs and checked whether it would affect the cellular level of MUC1. To improve experimental validation, two different siRNAs targeting different regions of human TRS were utilized. Both of the siRNAs targeting TRS appears to significantly reduced MUC1 and MUC1-CT levels when compared to non-targeting siRNA (Figure 3a). There were no changes observed in MUC1 mRNA under the same conditions (Figure 3b). To determine the TRS dependency on MUC1 levels, Panc 10.05 cells were transfected with siRNA targeting TRS or alanyl-tRNA synthetase (AlaRS) and specific reduction of MUC1 and MUC1-CT levels were observed in cells treated with siTRS, but not with siAlaRS (Figure 3c). The next was to examine how the suppression of TRS or AlaRS would affect global protein synthesis using a SUnSET technique (23) since they are protein synthesis enzymes. For this approach, Panc

10.05 cells transfected with siRNA were incubated with a low dose of puromycin (1 μM), which was incorporated into newly synthesized polypeptide chains. Newly synthesized proteins labelled with puromycin were quantified by immunoblotting of the whole cell lysates. The results showed no changes among siCON-, siTRS- and siAlaRS-treated cells in the amounts of newly synthesized proteins while CHX treatment completely block *de novo* protein synthesis (Figure 3d). In this condition, threonylation activity was only decreased in the cells transfected with siTRS, but not with siAlaRS (Figure 3e). It was also important to evaluate total protein synthesis at different times (24, 48, and 72 hrs) after the transfection of siRNAs using [^{35}S]Met incorporation assay. The protein levels of TRS and AlaRS were decreased in the siRNA-treated cells, but global protein synthesis was not significantly impacted despite the reduction of TRS or AlaRS protein levels. These results indicate that suppression of TRS specifically reduced biosynthesis of threonine-rich MUC1, not affecting global protein synthesis. To evaluate the effects of TRS on MUC1 protein level, two types of pancreatic cancer cells were generated expressing TRS shRNA or Myc-tagged TRS induced by doxycycline (Dox). To induce the target genes, pancreatic cancer cells were incubated with Dox (10 ng/ml) for 24 hrs. The silencing of TRS following Dox treatment resulted in a marked decrease in the level of MUC1 and MUC1-CT in Panc 10.05 and AsPC-1 cells (Figure 3f). On the other hand, overexpression of TRS by Dox induction resulted in a significant increase in the level of MUC1 and MUC1-CT in MIA PaCa2 and PANC-1 cells (Figure 3g). These data suggest that TRS specifically regulates biosynthesis of MUC1.

TRS inhibitors suppress pancreatic cancer cell migration

Next, to investigate whether the inhibition of TRS catalytic activity would also affect MUC1 level, the TRS activity was inhibited with the macrolide antibiotic, borrelidin (BN), a potent non-competitive inhibitor of TRS, and 5'-O-(N-(L-threonyl)-sulfamoyl) adenosine (ThrAMS), a non-hydrolyzable analog of the reaction intermediate, threonyl-adenylate. In the aminoacylation assay with human TRS, activity was decreased by ThrAMS treatment in a dose-dependent manner with an estimated IC_{50} of 245 nM (Figure4a, left). Previous studies have shown that BN inhibits the threonine activation step of human TRS with an inhibition constant (Ki) value of about 7 nM (Figure4a, right) (24). Panc 10.05 and AsPC-1 cells were then treated with different doses of BN and ThrAMS to investigate how they would affect MUC1 levels by Western blotting. The results show a dose-dependent decrease of MUC1 and MUC1-CT levels in these cells (Figure 4b and c). To see whether TRS inhibitors would affect the growth and migration of pancreatic cancer cells, cell growth and wound healing assays were performed. When Panc 10.05 cells were treated with different doses of BN or ThrAMS for 12 hrs, both of BN and ThrAMS dramatically inhibited cell migration (Figure 4d and e), with little effect cell growth (Figure 4f and g). Collectively, these results suggest the significance of TRS activity for biosynthesis of the protein MUC1.

TRS affects pancreatic cancer cell migration

The idea arose to utilize the two Dox-inducible TRS knockdown and overexpression cell lines that were used above to confirm that TRS-dependent MUC1 synthesis would affect pancreatic cancer cell migration. MUC1 and MUC1-CT protein level were significantly

reduced in 24 hrs after the TRS suppression (Figure 5a). Unsurprisingly, treatment of siRNA targeting MUC1 in shTRS-induced Panc 10.05 cells also decreased MUC1 and MUC1-CT protein levels (Figure 5a). Interestingly, suppression of TRS or MUC1 decreased Panc 10.05 cell migration to similar extents (Figure 5b and c) with little effect on cell growth (Figure 5d). On the contrary, there was an observed increase in MUC1 and MUC1-CT levels, following induction of Myc-TRS but not when MUC1 was suppressed with its specific siRNA (Figure 5e). MIA PaCa-2 cell migration was increased when Myc-TRS was induced, but decreased after treatment with siMUC1 (Figure 5f and g) without affecting cell growth (Figure 5h). Taken together, this data indicate that TRS could affect pancreatic cancer cell migration by regulating protein levels of MUC1.

TRS and MUC1 levels are positively correlated with pancreatic cancer.

The next step was to understand whether expression of TRS and MUC1 would show any relevance to the survival of pancreatic cancer patients. This required bioinformatics analysis using SynTarget, a new online tool that interrogates the expression of multiples genes from microarray datasets for synergistic survival relationships (Figure 6a) (25, 26). Interestingly, co-expression of TRS and MUC1 at high levels showed a positive correlation with poor survival outcomes of the patients (Figure 6b). On the contrary, when the expression of both TRS and MUC1 was low, patient survival was significantly improved (Figure 6c). To further assess the correlation between MUC1 and TRS levels in clinical pancreatic tumors, it was important to analyze the tissue levels of the two proteins using a tumor

microarray (TMA) including 30 clinical pancreatic tumor samples. Immunohistochemical signals of MUC1 and TRS were scored by the staining intensity and it was found that tissue samples with high levels of both TRS and MUC1 accounted for 60% of the total tissue samples. (Figure 6d). Moreover, strong staining of MUC1 and TRS was observed in the duct region of tumor samples, whereas no staining was observed in the duct region of normal samples (Figure 6e). These results support the notion that higher expression of TRS would increase MUC1 level, contributing to poor survival of pancreatic cancer patients.

Figure II-1. MUC1 protein levels in pancreatic cancer cells after threonine deprivation
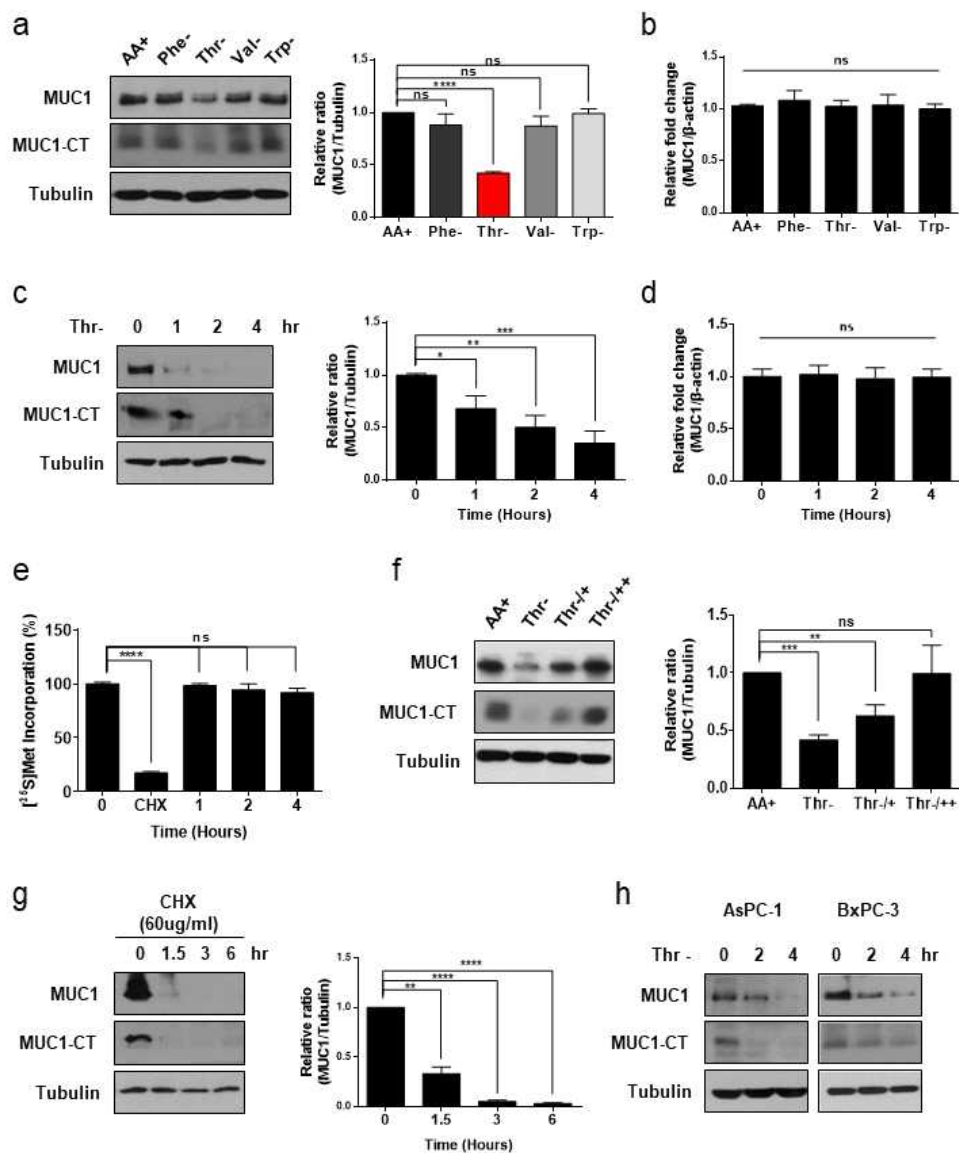
(a) Panc 10.05 cells were maintained in DMEM (AA+) or were deprived of all amino acids (AA−), phenylalanine (Phe−), Threonine (Thr−), Valine (Val−) or Tryptophan (Trp−) for 2 hr. MUC1 and MUC1−CT protein levels were evaluated by immunoblotting (left) and displayed as a bar graph after calibration with tubulin levels (right).

(b) Effects of amino acids deprivation on MUC1 transcription were evaluated by quantitative RT−PCR analysis in Panc 10.05 cells.

(c) Panc 10.05 cells were deprived of threonine (Thr−) for 1 to 4 hrs. MUC1 and MUC1−CT protein levels were evaluated by immunoblotting (left) and displayed as a bar graph after calibration with tubulin levels (right).

(d) Effects of threonine starvation on MUC1 transcription were evaluated by qRT−PCR analysis in Panc 10.05 cells.

(e) Panc 10.05 cells were incubated with [^{35}S]Met with or without threonine in a time dependent manner. Protein synthesis was monitored by the [^{35}S]−Met incorporation assay and displayed as a bar graph.

(f) Panc 10.05 cells were cultured in media containing (AA+) or lacking threonine (Thr−) for 2 hrs. After withdrawal for 2 hrs, threonine−containing media was added for 1 or 2 hrs (Thr−/+ or Thr−/++). MUC1 and MUC1−CT protein levels were evaluated by immunoblotting (left) and displayed as a bar graph (right).

(g) Panc 10.05 cells were treated with 60 μg/ml cycloheximide (CHX)

for 1 to 4 hr and protein levels of MUC1 and MUC1-CT were evaluated by immunoblotting with anti-MUC1 antibody (left) and displayed as a bar graph (right).

(h) Immunoblotting analysis of the MUC1 and MUC1-CT in lysates of AsPC-1 and BxPC-3 cells that were deprived threonine (Thr-) for 2 to 4 hrs.

(a – g) *, $p < 0.05$; **, $p < 0.01$; ***, $p < 0.001$; ****, $p < 0.0001$; NS, not significant vs. control group. Values are means ± SEM of three independent experiments.

Figure II-2. Effects of threonine deprivation on pancreatic cancer cell migration
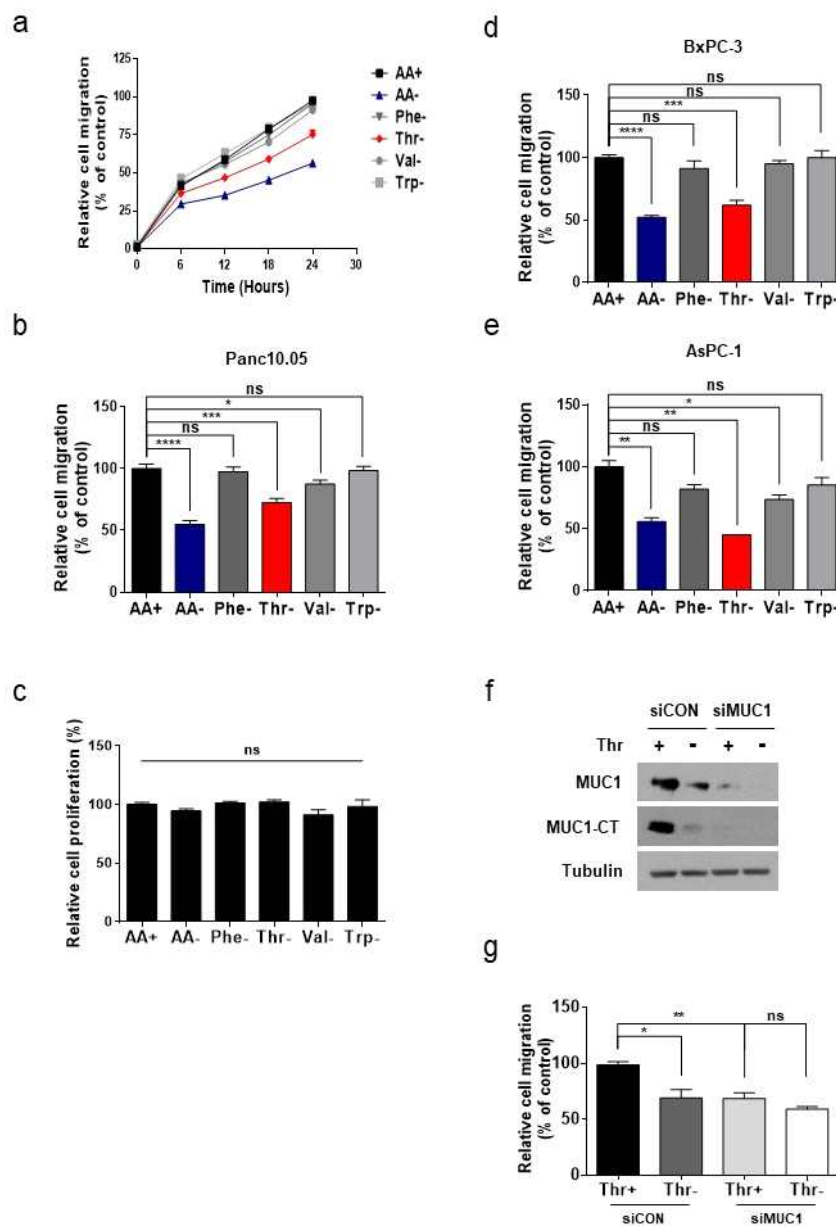
(a) Panc 10.05 cells were seeded at equal densities into 96-well plates, cultured to confluency, mechanically wounded by scratching, incubated in each medium and then monitored for 24 hrs by IncuCyte Zoom^{TM}.Thedataisdisplayedaslinegraphs.

(b) Quantification of migration of Panc 10.05 cells treated as described in (a) for 24 hrs. Migration distance was measured using the IncuCyte software and displayed as a bar graph.

(c) Panc 10.05 cells were seeded at equal densities into 96-well plates, imaged within the IncuCyte Zoom^{TM}, and analyzed as percentage confluence. The data displayed as a bar graph.

(d – e) Quantification of migration of AsPC-1 (d) and BxPC-3 (e) cells treated as described in (a) for 24 hrs. Migration distance was measured using the IncuCyte software and displayed as a bar graph.

(f) Panc 10.05 cells were transfected with non-targeting or MUC1 targeting siRNAs for 24 hrs and then incubated in media with or without threonine for 24 hrs. Protein levels of MUC1 and TRS were monitored by immunoblotting with each antibody.

(g) Panc 10.05 cells were seeded at equal densities into 96-well plates, cultured to confluency, mechanically wounded by scratching, incubated in medium with or without threonine and then monitored for 24 hrs by IncuCyte Zoom^{TM}. Cell migration was quantified based on the distance separating wound images and displayed as a bar graph.

(a – e, and g) *, p < 0.05; **, p < 0.01; ***, p < 0.001; ****, p < 0.0001; NS, not significant vs. control group. Values are means ± SEM of three independent experiments.

Figure II-3. MUC1 biosynthesis via TRS in pancreatic cancer cells
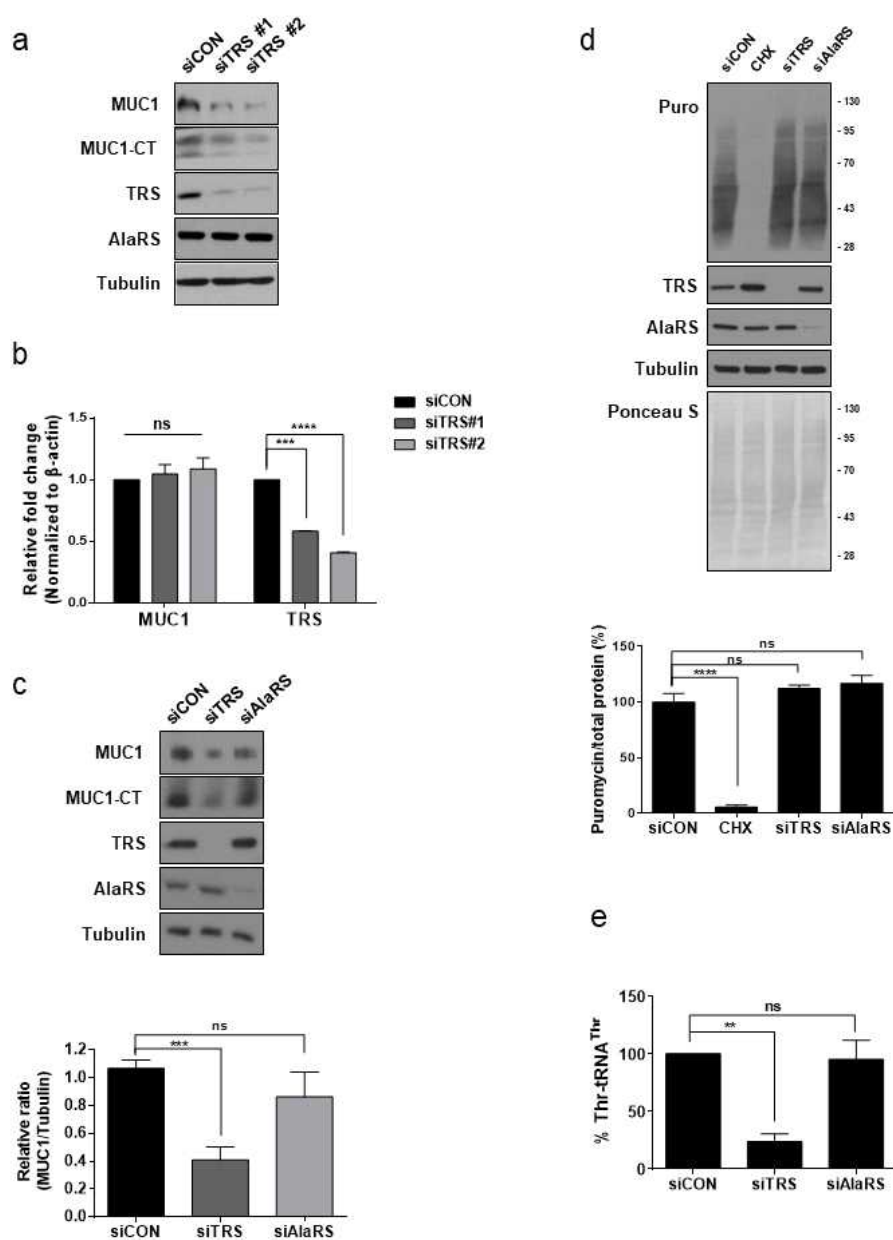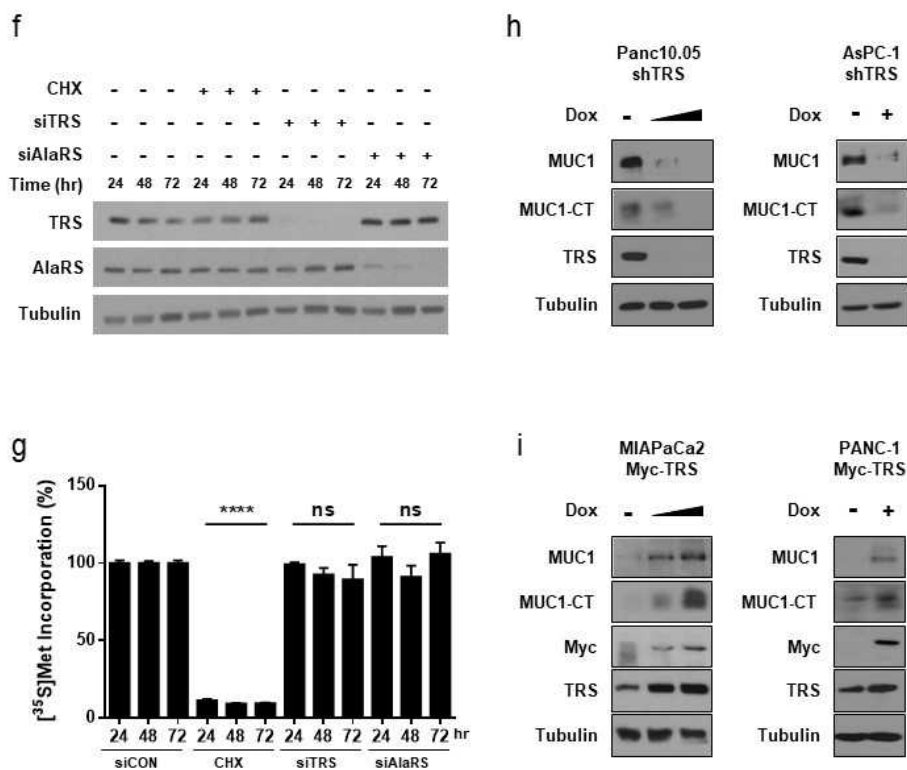
(a) TRS was suppressed with two different siRNAs for 48 hrs in Panc 10.05 cells and protein levels of MUC1 and MUC1-CT were evaluated by immunoblotting with anti-MUC1 antibody. AlaRS and tubulin were used as controls. siCON, non-targeting control siRNA.

(b) Effects of TRS suppression on the transcription levels of MUC1 and TRS were analyzed by qRT-PCR with the primers targeting TRS and MUC1.

(c) TRS and AlaRS were suppressed with their specific siRNAs for 48 hrs in Panc 10.05 cells and protein levels of MUC1 and MUC1-CT

were evaluated by immunoblotting with anti-MUC1 antibody (top) and displayed as a bar graph (bottom).

(d) TRS and AlaRS were suppressed with their specific siRNAs for 48 hrs in Panc 10.05 cells and treated with puromycin (1μM) for 30 mins. *De novo* global protein synthesis was then monitored by immunoblotting of cell lysates with anti-puromycin antibody. The proteins were quantified by Ponceau S staining. CHX was employed as a positive control to block *de novo* protein synthesis (top).The ratio of *de novo* protein synthesis versus global protein synthesis was determined as a percentage and shown as a bar graph (bottom).

(e) Panc 10.05 cells were transfected with siRNAs against TRS, AlaRS, or a non-targeting control, and the catalytic activities of cell lysates were determined by threonylation of tRNA^{Thr} as described in Methods. The amount of threonine-charged tRNAs was measured by scintillation counting and the data were displayed as a bar graph.

(f) Panc 10.05 cells were transfected with siTRS or siAlaRS in a time dependent manner and protein levels of TRS and AlaRS were evaluated by immunoblotting using anti-TRS or anti-AlaRS antibodies. CHX was used as positive control and treated for 30 mins.

(g) Protein synthesis was measured in Panc 10.05 cells transfected with siCON, siTRS, or siAlaRS in a time dependent manner by [^{35}S]Met incorporation assay. Data were displayed as a bar graph. CHX was used as a positive control and treated for 30mins.

(h) Panc 10.05 and AsPC-1 cells that expressed inducible shRNA targeting TRS were cultured in the presence or absence of Doxycycline (Dox) for 24 to 48 hrs. Expression of MUC1, MUC1-CT, and TRS were determined by immunoblotting using anti-MUC1 or anti-TRS antibodies.

(i) MIA PaCa-2 and PANC-1 cells that expressed inducible myc-tagged TRS were cultured in the presence or absence of Dox for 24 to 48 hrs. Expression of MUC1, MUC1-CT, and myc-tagged TRS were detected by immunoblotting with each antibody.

(b – e, and g) **, $p < 0.01$; ***, $p < 0.001$; ****, $p < 0.0001$; NS, not significant vs. control group. Values are means ± SEM of three independent experiments.

Figure II-4. Effects of TRS inhibitor on pancreatic cancer cell migration
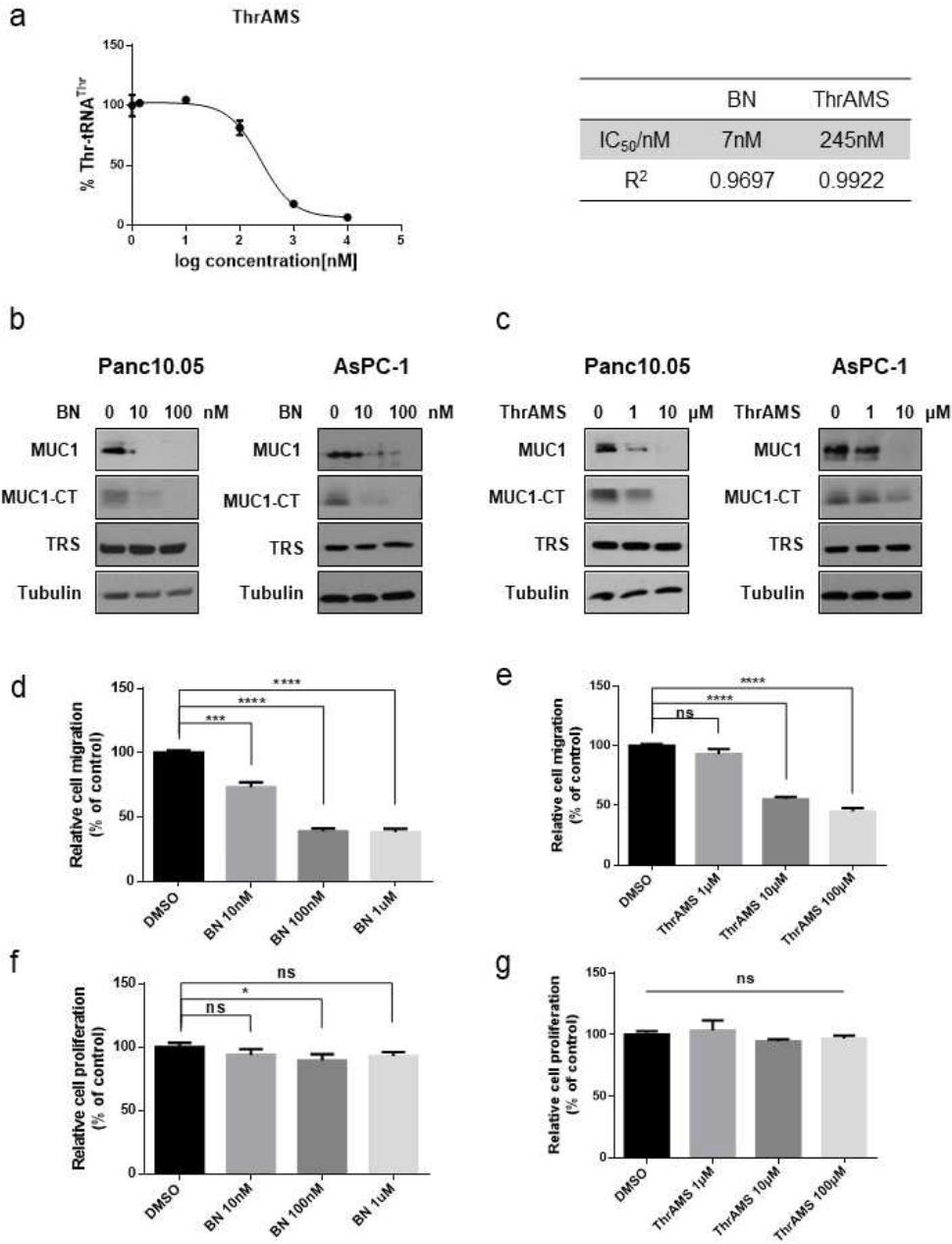
(a) Aminoacylation activity of recombinant human TRS protein was assayed with ThrAMS titration (10 – 10,000 nM), with an estimated IC_{50} of 245nM. The activity was normalized to DMSO, which is used as the solvent for ThrAMS. ThrAMS, 5'-O-(N-(L-threonyl)-sulfamoyl) adenosine; BN, Borrelidin.

(b) Panc 10.05 and AsPc-1 cells were treated with the indicated concentration (10 and 100 nM) of BN for 4 hrs. Protein levels of MUC1, MUC1-CT, and TRS were monitored by immunoblotting with each antibody.

(c) Panc 10.05 and AsPC-1 cells were treated with the indicated concentration (1 and 10 µM) of ThrAMS for 4 hrs. Protein levels of MUC1, MUC1-CT, and TRS were monitored by immunoblotting with each antibody.

(d) Panc 10.05 cells were seeded at equal densities into 96-well plates, cultured to confluency, mechanically wounded by scratching, incubated in medium with indicated concentration (10 nM to 1 µM) of BN and then monitored for 12 hrs by IncuCyte Zoom^{TM}. Cell migration was quantified based on the distance separating wound images and displayed as a bar graph.

(e) Panc 10.05 cells were seeded at equal densities into 96-well plates, cultured to confluency, mechanically wounded by scratching, incubated in medium with indicated concentration (1 µM to 100 µM) of ThrAMS and then monitored for 12 hrs by IncuCyte Zoom^{TM}. Cell migration was quantified based on the distance separating wound
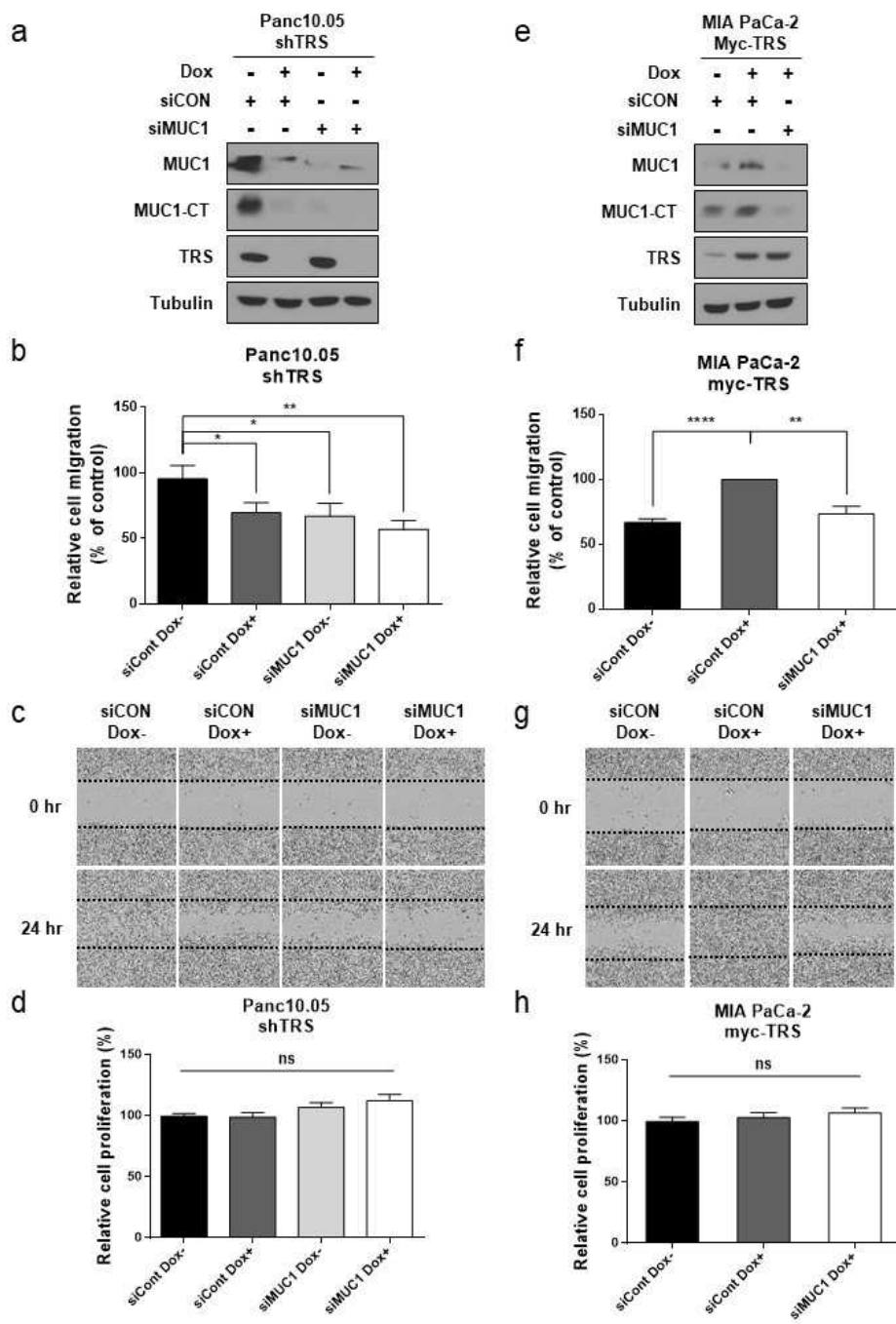
images and displayed as a bar graph.

(f) Panc 10.05 cells were seeded at equal densities into 96-well plates with indicated concentration (10 nM to 1 μM) of BN and imaged within the IncuCyte Zoom^{TM}. Proliferation was analyzed as percentage confluence and displayed as a bar graph.

(g) Panc 10.05 cells were seeded at equal densities into 96-well plates with indicated concentration (1 μM to 100 μM) of ThrAMS and imaged within the IncuCyte Zoom^{TM}. Proliferation was analyzed as percent confluence and displayed as a bar graph.

(d – g) *, $p < 0.05$; ***, $p < 0.001$; ****, $p < 0.0001$; NS, not significant vs. control group. Values are means ± SEM of three independent experiments.

Figure II-5. Effects of TRS on pancreatic cancer cell migration

(a – d) Panc 10.05 cells were transfected with non-targeting or MUC1 targeting siRNAs for 24 hrs and then treated with Dox for 24 hrs to induce shRNA specific to TRS.

(a) Protein levels of MUC1 and TRS were monitored by immunoblotting with each antibody.

(b) Panc 10.05 cells were seeded at equal densities into 96-well plates, cultured to confluency, mechanically wounded by scratching, incubated in medium and then monitored for 24 hrs by IncuCyte Zoom^{TM}. Cell migration was quantified based on the distance separating wound images and displayed as a bar graph.

(c) Light microscopy images depicting migration in wound healing assay as described in (b). Images were captured at 0 hrs (top) and 24 hrs (bottom) and showed the wound gap filled by cells after scratching.

(d) Panc 10.05 cells were seeded at equal densities into 96-well plates and imaged within the IncuCyte Zoom^{TM}. Proliferation was analyzed as percent confluence and displayed as a bar graph.

(e – h) MIA PaCa-2 cells were transfected with non-targeting or MUC1 targeting siRNAs for 24 hrs and then treated with Dox for 24 hrs to induce myc-tagged TRS.

(e) Protein levels of MUC1 and TRS were monitored by immunoblotting with each antibody.

(f) MIA PaCa-2 cells were seeded at equal densities into 96-well

plates, cultured to confluency, mechanically wounded by scratching, incubated in medium and then monitored for 24 hrs by IncuCyte Zoom^{TM}. Cell migration was quantified based on the distance separating wound images and displayed as a bar graph.

(g) Light microscopy images depicting migration in wound healing assay as described in (f). Images were captured at 0 hr (top) and 24 hr (bottom) and showed the wound gap filled by cells after scratching.

(h) MIA PaCa-2 cells were seeded at equal densities into 96-well plates and imaged within the IncuCyte Zoom^{TM}. Proliferation was analyzed as percentage confluence and displayed as bar graph.

(b – d, and f – h) *, $p < 0.05$; **, $p < 0.01$; ****, $p < 0.0001$; NS, not significant vs. control group. Values are means ± SEM of three independent experiments. All images were captured by IncuCyte ZOOM^{TM}.
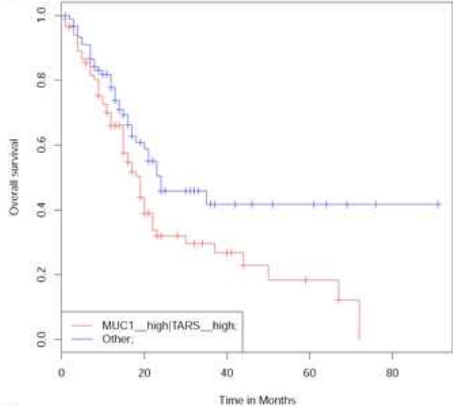
Figure II-6. Positive correlation between MUC1 and TRS in pancreatic cancer
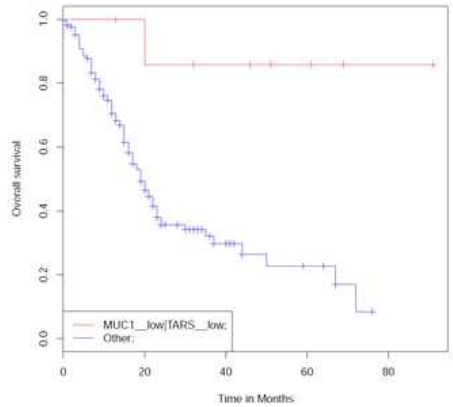
(a) Positive correlation between MUC1/TRS co-expression and survival effect of pancreatic cancer patients dataset from TCGA. (GEO dataset ID: TCGA_PAAD)

(b, c) The bioinformatics analysis of synergetic effects of MUC1 and TRS co-expression with overall survival in months within human pancreatic adenocarcinoma patients with (b) high MUC1 and high TRS expression (**, $p < 0.01$) or (c) with low MUC1 and low TRS expression (*, $p < 0.05$).

(d) Summary table of the quantitative expression of MUC1 and TRS with the score of the respective pancreatic adenocarcinoma tissue microarray (TMA). A TMA of pancreatic adenocarcinomas was immunostained with antibodies against MUC1 and TRS, respectively. Immunohistochemical (IHC) signals were scored by the staining intensity (0: no signal, 1: weak signal, 2: intermediate signal, and 3: strong signal). Low, 0-1; high, 2-3.

(e) Representative examples of patient biopsies of pancreatic adenocarcinoma assembled into a TMA stained for MUC1 and TRS, depicting the reciprocal expression pattern (x5) (top). Boxed areas are shown at higher magnification (x20) (bottom). Scale bar (x5), 500 μm; scale bar (x20), 100 μm.

Discussion

The oncoprotein MUC1 is overexpressed in 90% of pancreatic cancers and associated with a short survival rate (27, 28). MUC1 also induces epithelial-mesenchymal transition as well as increased cell invasion (29). For these reasons, MUC1 is considered an attractive target to moderate pancreatic cancer progression. In this study, deprivation of threonine (Figure 1), reduction of TRS expression (Figure 3) and catalytic activity (Figure 4) have been associated with decreased MUC1 levels, and consequently, the suppression of pancreatic cancer cell migration. A number of preclinical studies suggest that decreasing mucin expression in tumors has potential as a novel molecular approach for the treatment of pancreatic cancer (30-33). Since MUC4 and MUC16 are also threonine-rich glycoproteins, their cellular levels are also presumably regulated by TRS in pancreatic cancer cells (34-37).

Previous reports showed that threonine is considered an essential amino acid important for mucin synthesis (13-17). In line with previous studies, work presented here indicates that threonine supplementation is critical for MUC1 oncoprotein biosynthesis in pancreatic cancer cells (Figure 1).

Many reports show the functional implications of human aminoacyl-tRNA synthetases (ARSs) for cancer growth and progression via their unique activities unassociated with catalysis (38-41). However, it is unknown whether the increased expression of ARSs would catalytically contribute to tumorigenesis. Presented in this study is the first report showing that the biosynthesis of mucin

can be controlled by the inhibition of TRS activity or by the suppression of TRS expression without affecting global protein synthesis. TRS expression was increased in ovarian cancer and suggested to be associated with angiogenesis (42). However, it may be related to the unique activity of the secreted TRS in the extracellular space since it was previously shown that TRS can be secreted to promote angiogenesis (43). Considering that TRS specifically regulates biosynthesis of threonine-rich protein, MUC1, it would be interesting to investigate whether specific amino acid-rich proteins can be also specifically regulated by their cognate ARSs.

ARSs are validated drug targets against pathogens (44, 45). Recently, there are increasing efforts to target human ARSs for various pharmacological indications (46, 47). For instance, halofuginone (HF), the halogenated derivative of febrifugine, has been tested for fibrosis treatment (48). Accumulation of extra cellular matrix proteins, especially collagen, is a main feature of fibrotic disease. Since collagen is a proline-rich protein, prolyl-tRNA synthetase (PRS) could serve as a preferred target to block collagen biosynthesis. In fact, HF, the specific PRS inhibitor showed high efficacy to decrease collagen level (49, 50).

In summary, this study provides evidence illuminating the potential role of TRS in the migration of human pancreatic cancer cells by enhancing MUC1 biosynthesis. The effect of TRS inhibitors on MUC1 levels and cancer cell migration suggests the possibility of TRS as a novel target against pancreatic cancer. However, further validation studies are currently under way using in vivo models and patient analysis.

Materials and Methods

Materials

Anti-MUC1 (cat# ab109185) was purchased from abcam (Cambridge, UK), anti-MUC1 (cat# sc-7313), anti-ThrRS (cat# sc-166146), anti-c-Myc (cat# sc-40), and anti-AlaRS (cat# sc-98547) were purchased from Santa Cruz Biotechnology (Dallas, TX, USA), anti-alpha-tubulin (cat# T6074) was purchased from Sigma-Aldrich (St Louis, MO, USA), and anti-puromycin (cat# MABE343) was purchased from Millipore (Billerica, MA, USA). L-[^{35}S]-Methionine (Met) (cat# NEG709A) was purchased from PerkinElmer (Waltham, MA, USA). Threonine, L-[3-3H] (cat# ART0330) was purchased from American Radiolabeled Chemicals (Saint Louis, MO, USA). Borrelidin (cat# ab144212) was purchased from abcam. 5'-O-(N-(L-threonyl)-sulfamoyl) adenosine was purchased from Integrated DNA Technologies (Coralville, IA, USA). Lipofectamine 2000 (cat# 11668030) and puromycin (cat# A1113802) were purchased from Thermo Fisher (Waltham, MA, USA).

Cell culture

PANC-1, MIA PaCa-2 and HEK293T cells were cultured in high glucose Dulbecco's Modified Eagle's Medium (Hyclone, Logan, UT, USA) with 10% fetal bovine serum (FBS) (Hyclone) and 1% streptomycin and penicillin (S/P) (Hyclone). AsPC-1, Panc 10.05 and

BxPC-3 cells were cultured in Roswell Park Memorial Institute 1640 (Hyclone) with 10% FBS and 1% S/P. HPAF-II cells were cultured in Eagle's Minimum Essential Medium (Hyclone) with 10% FBS and 1% S/P. CFPAC-1 cells were cultured in Iscove's Modified Dulbecco's Medium (Hyclone) with 10% FBS and 1% S/P. Cells were incubated in a humidified atmosphere at 37 ℃ in 5% carbon dioxide (CO_2).

Threonine starvation of cells

For threonine depletion, cells were rinsed with threonine-free medium (WelGENE, Daegu, Korea) twice, and incubated in threonine-free medium for the indicated time. For wound healing assays, cells were rinsed with threonine-free medium twice, incubated for the indicated time in threonine-free medium containing dialyzed FBS (Hyclone) after making scratches.

Preparation of cell lysates and immunoblotting

Cells were dissolved in lysis buffer containing 1% Triton X-100, 50 mM HEPES (pH 7.4), 2 mM EDTA, 10 mM pyrophosphate, 10 mM glycerophosphate, protease inhibitor cocktail (Calbiochem, San Diego, CA, USA), and lysates were centrifuged at 13,000 rpm for 15 min. Then, 20 mg of the extracted proteins were fractionated by sodium dodecyl sulfate-polyacrylamide gel electrophoresis (SDS-PAGE). Immunoblotting was performed according to previously described methods using specific antibodies.[19]

Quantitative real-time polymerase chain reaction

Total RNA was extracted from cells using the RNeasy Kit (QIAGEN, Hilden, Germany) according to the manufacturer's instructions and the purified RNAs were used for cDNA synthesis using a PrimeScript RT reagent kit (TaKaRa, Shiga, Japan). Quantitative polymerase chain reaction (PCR) was performed using gene-specific primer sets and SYBR Green Supermix (Biorad, Hercules, CA, USA). Real-time PCR was carried out in a 7500 real-time PCR system (Applied Biosystems, Foster city, CA, USA) according to the manufacturer's instructions. Data were normalized against β-actin mRNA levels. Relative expression was calculated using the DDCT method. PCR was performed using the human MUC1 primer set (forward primer: 5'-GAACTACGGGCAGCTGGACATC-3', reverse primer: 5'-GCTCTCTGGGCCAGTCCTCCTG-3') or the human TRS primer set (forward primer: 5'-GTAAGCCATGATGGTG-3', reverse primer: 5'-CTGCCTGTTTGCTGCGG-3') and the β-actin primer set (forward primer: 5'-GAGCTGCCTGACGGCCAGG-3', reverse primer: 5'-CATCTGCTGGAAGGTGGAC-3').

[^{35}S]-MetIncorporationassay

Cells were seeded into 24-well plates, grown until subconfluent and incubated in Met-free media containing 10 mCi/ml [^{35}S]-Met for 1hr. The cells were then washed twice with ice-cold PBS, treated with 5 % trichloroaceticacid (TCA) for 30 min, washed twice with ice-cold PBS and solubilized in 0.5 N NaOH, and an aliquot was counted by

liquid scintillation counter (Beckman Coulter, Brea, CA, USA).

Wound healing assay

Wound healing assays were performed with the IncuCyte^{TM} Zoom according to the supplier's protocols. Cells were seeded in 96-well ImageLock plates (EssenBioScience, AnnArbor, MI, USA) and grown to 90 - 95 % confluency. Subsequently, a WoundMaker (EssenBioscience) was used to create scratches in all of the wells, once the media was replaced, images of cell migration were recorded every 2 hrs for a total duration of 48 hrs by the IncuCyte Kinetic Live Cell Imaging System and analyzed with the IncuCyte Zoom software.

Cell proliferation analysis

Cells were seeded in triplicate using a 96-well plate at a density of 5,000 cells per well and placed within a microplate tray of IncuCyte^{TM} ZOOM (EssenBioScience). Cells were monitored every 2 hrs for a total duration of 72 hrs using the IncuCyte Kinetic Live Cell Imaging System (EssenBioScience) and analyzed with the IncuCyte Zoom software (EssenBioScience).

RNA interference

Cells were transfected with duplex siRNA using the Lipofectamine 2000 transfection reagent (Invitrogen, Carlsbad, CA, USA) according to the manufacturer's instructions. ON-TARGETplus SMARTpool

siRNAs against TRS (cat# L-011789) and AlaRS (cat# L-011565) were purchased from GE Healthcare Dharmacon (Lafayette, CO, USA). A non-targeting siRNA was used as a control (Dharmacon). Double-stranded siRNAs targeting human TRS (5''-TCGCTTTCGGGTTCTCTCATCGCTT-3'), MUC1 (5'-GGUAAUGGUGGCAGCAGCCUCUCUU-3') were purchased from Invitrogen. Cells were incubated with the siRNA for 36-72 hr.

Puromycin incorporation assay

Surface sensing of translation (SUnSET) was performed as previously described.[20] Briefly, cells were incubated with 1 μM puromycin (Thermo Fisher) for 30 min followed by washing with ice cold PBS and lysing with lysis buffer. We loaded cell lysates onto SDS-PAGE, performed western blots with mouse anti-puromycin monoclonal antibody (Millipore), and normalized against Ponceau S staining (INtRON, Gyeongggi-do, Korea).

Aminoacylation assay

Aminoacylation assays were performed as previously described.[21] Briefly, assays were carried out in a buffer containing 4 mM DTT, 50 mM HEPES-KOH (pH 7.6), 20 mM KCl, 10 mM $MgCl_2$, 5 mM ATP, 2 mg/ml yeast tRNA (Roche, Indianapolis, IN, USA), threonine, L-[3-3H] (American Radiolabeled Chemicals), and cell lysates. Reactions were initiated with cell lysates and conducted at 37°C. Aliquots (20 ml) were taken from the reactants after 30 min and

quenched on Whatman filter pads that were presoaked with 5% TCA. Pads were washed three times for 10 min each time with cold 5% TCA, and once with cold 100% ethanol. Washed pads were then dried, and radioactivity was quantified using a scintillation counter (Beckman Coulter, Brea, CA, USA)

Establishment of doxycycline-inducible cell line

Pancreatic cancer cells were seeded evenly in a 60 mm dish and incubated for 12 hrs to reach approximately 90% conflueec. When the cells were ready for transfection, 2 μL of shTRS or myc-TRS lentiviral particles and 3 μL of 10 mg/mL polybrene were supplemented with 2 mL of complete media and added to plate. After 16 hrs of incubation, the culture media was replaced with 3 mL of fresh complete media containing 1 μg/mL puromycin and incubated for an additional 48 hrs. The cells were gradually selected by treating puromycin every 48 hrs. To check the efficiency of TRS knockdown or overexpression, treatment with 2.5 μg/mL of doxycycline (Dox) occurred for the indicated time and immunoblotting was performed. shTRS was purchased from Dharmacon.

SynTarget software

Correlations of expression levels from MUC1 and TRS with the survival rates of pancreatic cancer patients were analyzed by SynTarget Software (http://www.chemoprofiling.org/cgi-bin/GEO/cancertarget/web_run_CT.

V0.S1.pl) using publically available Gene Expression Omnibus (GEO) dataset (GEO dataset ID: TCGA_PAAD).

Tissue microarrays

Commercially available tissue microarray sections of human PDACs (Cat# A307II AccuMax Array) were purchased from ISU ABXIS (Seoul, Korea) and used according to the manufacturer's instructions. Slides were analyzed by bright-field microscopy using Pannoramic 250 1.14 slide scanner and Pannoramic Viewer 1.15 (3DHISTECH, Budapest, Hungary).

Statistical analysis

Statistical analyses were performed using Prism6 (GraphPad Software, San Diego, CA, USA). All data values are represented as mean ± SEM and statistical significance was denoted as follow: ns, Not significant, $p \geq 0.05$; *, $p < 0.05$; **, $p < 0.01$; ***, $p < 0.001$; ****, $p < 0.0001$.

References

1. Schneider G, Siveke JT, Eckel F, Schmid RM. Pancreatic cancer: basic and clinical aspects. Gastroenterology. 2005;**128**:1606-25.

2. Vincent A, Herman J, Schulick R, Hruban RH, Goggins M. Pancreatic cancer. Lancet. 2011;**378**:607-20.

3. Wong HH, Lemoine NR. Pancreatic cancer: molecular pathogenesis and new therapeutic targets. Nat Rev Gastroenterol Hepatol. 2009;**6**:412-22.

4. Gendler SJ. MUC1, the renaissance molecule. J Mammary Gland Biol Neoplasia. 2001;**6**:339-53.

5. Kufe DW. Mucins in cancer: function, prognosis and therapy. Nat Rev Cancer. 2009;**9**:874-85.

6. Singh PK, Hollingsworth MA. Cell surface-associated mucins in signal transduction. Trends Cell Biol. 2006;**16**:467-76.

7. Nath S, Mukherjee P. MUC1: a multifaceted oncoprotein with a key role in cancer progression. Trends Mol Med. 2014;**20**:332-42.

8. Horm TM, Schroeder JA. MUC1 and metastatic cancer: expression, function and therapeutic targeting. Cell Adh Migr. 2013;**7**:187-98.

9. Van Klinken BJ, Dekker J, Buller HA, Einerhand AW. Mucin gene structure and expression: protection vs. adhesion. Am J Physiol. 1995;**269**:G613-27.

10. Mantle M, Allen A. Isolation and characterization of the native glycoprotein from pig small-intestinal mucus. Biochem J. 1981;**195**:267-75.

11. Schaart MW, Schierbeek H, van der Schoor SR, Stoll B, Burrin DG, Reeds PJ, et al. Threonine utilization is high in the intestine of piglets. J Nutr. 2005;**135**:765-70.

12. van der Schoor SR, Wattimena DL, Huijmans J, Vermes A, van

Goudoever JB. The gut takes nearly all: threonine kinetics in infants. Am J Clin Nutr. 2007;**86**:1132-8.

13. Faure M, Moennoz D, Montigon F, Mettraux C, Breuille D, Ballevre O. Dietary threonine restriction specifically reduces intestinal mucin synthesis in rats. J Nutr. 2005;**135**:486-91.

14. Law GK, Bertolo RF, Adjiri-Awere A, Pencharz PB, Ball RO. Adequate oral threonine is critical for mucin production and gut function in neonatal piglets. Am J Physiol Gastrointest Liver Physiol. 2007;**292**:G1293-301.

15. Wang X, Qiao S, Yin Y, Yue L, Wang Z, Wu G. A deficiency or excess of dietary threonine reduces protein synthesis in jejunum and skeletal muscle of young pigs. J Nutr. 2007;**137**:1442-6.

16. Nichols NL, Bertolo RF. Luminal threonine concentration acutely affects intestinal mucosal protein and mucin synthesis in piglets. J Nutr. 2008;**138**:1298-303.

17. van der Sluis M, Schaart MW, de Koning BA, Schierbeek H, Velcich A, Renes IB, et al. Threonine metabolism in the intestine of mice: loss of mucin 2 induces the threonine catabolic pathway. J Pediatr Gastroenterol Nutr. 2009;**49**:99-107.

18. Park SG, Ewalt KL, Kim S. Functional expansion of aminoacyl-tRNA synthetases and their interacting factors: new perspectives on housekeepers. Trends Biochem Sci. 2005;**30**:569-74.

19. Baliga BS, Pronczuk AW, Munro HN. Mechanism of cycloheximide inhibition of protein synthesis in a cell-free system prepared from rat liver. J Biol Chem. 1969;**244**:4480-9.

20. Besmer DM, Curry JM, Roy LD, Tinder TL, Sahraei M, Schettini J, et al. Pancreatic ductal adenocarcinoma mice lacking mucin 1 have a profound defect in tumor growth and metastasis. Cancer Res. 2011;**71**:4432-42.

21. Kitamoto S, Yokoyama S, Higashi M, Yamada N, Takao S, Yonezawa S. MUC1 enhances hypoxia-driven angiogenesis through the regulation of multiple proangiogenic factors. Oncogene. 2013;**32**:4614-21.

22. Liu X, Yi C, Wen Y, Radhakrishnan P, Tremayne JR, Dao T, et al. Interactions between MUC1 and p120 catenin regulate dynamic features of cell adhesion, motility, and metastasis. Cancer Res. 2014;**74**:1609-20.

23. Schmidt EK, Clavarino G, Ceppi M, Pierre P. SUnSET, a nonradioactive method to monitor protein synthesis. Nat Methods. 2009;**6**:275-7.

24. Fang P, Yu X, Jeong SJ, Mirando A, Chen K, Chen X, et al. Structural basis for full-spectrum inhibition of translational functions on a tRNA synthetase. Nat Commun. 2015;**6**:6402.

25. Antonov AV. BioProfiling.de: analytical web portal for high-throughput cell biology. Nucleic Acids Res. 2011;**39**:W323-7.

26. Amelio I, Tsvetkov PO, Knight RA, Lisitsa A, Melino G, Antonov AV. SynTarget: an online tool to test the synergetic effect of genes on survival outcome in cancer. Cell Death Differ. 2016;**23**:912.

27. Torres MP, Chakraborty S, Souchek J, Batra SK. Mucin-based targeted pancreatic cancer therapy. Curr Pharm Des. 2012;**18**:2472-81.

28. Kaur S, Kumar S, Momi N, Sasson AR, Batra SK. Mucins in pancreatic cancer and its microenvironment. Nat Rev Gastroenterol Hepatol. 2013;**10**:607-20.

29. Roy LD, Sahraei M, Subramani DB, Besmer D, Nath S, Tinder TL, et al. MUC1 enhances invasiveness of pancreatic cancer cells by inducing epithelial to mesenchymal transition. Oncogene. 2011;**30**:1449-59.

30. Singh AP, Moniaux N, Chauhan SC, Meza JL, Batra SK.

Inhibition of MUC4 expression suppresses pancreatic tumor cell growth and metastasis. Cancer Res. 2004;**64**:622-30.

31. Tsutsumida H, Swanson BJ, Singh PK, Caffrey TC, Kitajima S, Goto M, et al. RNA interference suppression of MUC1 reduces the growth rate and metastatic phenotype of human pancreatic cancer cells. Clin Cancer Res. 2006;**12**:2976-87.

32. Chaturvedi P, Singh AP, Moniaux N, Senapati S, Chakraborty S, Meza JL, et al. MUC4 mucin potentiates pancreatic tumor cell proliferation, survival, and invasive properties and interferes with its interaction to extracellular matrix proteins. Mol Cancer Res. 2007;**5**:309-20.

33. Yuan Z, Wong S, Borrelli A, Chung MA. Down-regulation of MUC1 in cancer cells inhibits cell migration by promoting E-cadherin/catenin complex formation. Biochem Biophys Res Commun. 2007;**362**:740-6.

34. Felder M, Kapur A, Gonzalez-Bosquet J, Horibata S, Heintz J, Albrecht R, et al. MUC16 (CA125): tumor biomarker to cancer therapy, a work in progress. Mol Cancer. 2014;**13**:129.

35. Garg G, Gibbs J, Belt B, Powell MA, Mutch DG, Goedegebuure P, et al. Novel treatment option for MUC16-positive malignancies with the targeted TRAIL-based fusion protein Meso-TR3. BMC Cancer. 2014;**14**:35.

36. Gautam SK, Kumar S, Cannon A, Hall B, Bhatia R, Nasser MW, et al. MUC4 Mucin- A Therapeutic Target for Pancreatic Ductal Adenocarcinoma. Expert Opin Ther Targets. 2017.

37. Rachagani S, Macha MA, Ponnusamy MP, Haridas D, Kaur S, Jain M, et al. MUC4 potentiates invasion and metastasis of pancreatic cancer cells through stabilization of fibroblast growth factor receptor 1. Carcinogenesis. 2012;**33**:1953-64.

38. Park SG, Schimmel P, Kim S. Aminoacyl tRNA synthetases and their connections to disease. Proc Natl Acad Sci U S A. 2008;**105**:11043-9.

39. Kim D, Kwon NH, Kim S. Association of aminoacyl-tRNA synthetases with cancer. Top Curr Chem. 2014;**344**:207-45.

40. Kim S, You S, Hwang D. Aminoacyl-tRNA synthetases and tumorigenesis: more than housekeeping. Nat Rev Cancer. 2011;**11**:708-18.

41. Kim YW, Kwon C, Liu JL, Kim SH, Kim S. Cancer association study of aminoacyl-tRNA synthetase signaling network in glioblastoma. PLoS One. 2012;**7**:e40960.

42. Wellman TL, Eckenstein M, Wong C, Rincon M, Ashikaga T, Mount SL, et al. Threonyl-tRNA synthetase overexpression correlates with angiogenic markers and progression of human ovarian cancer. BMC Cancer. 2014;**14**:620.

43. Williams TF, Mirando AC, Wilkinson B, Francklyn CS, Lounsbury KM. Secreted Threonyl-tRNA synthetase stimulates endothelial cell migration and angiogenesis. Sci Rep. 2013;**3**:1317.

44. Silvian LF, Wang J, Steitz TA. Insights into editing from an ile-tRNA synthetase structure with tRNAile and mupirocin. Science. 1999;**285**:1074-7.

45. Rock FL, Mao W, Yaremchuk A, Tukalo M, Crepin T, Zhou H, et al. An antifungal agent inhibits an aminoacyl-tRNA synthetase by trapping tRNA in the editing site. Science. 2007;**316**:1759-61.

46. Gadakh B, Van Aerschot A. Aminoacyl-tRNA synthetase inhibitors as antimicrobial agents: a patent review from 2006 till present. Expert Opin Ther Pat. 2012;**22**:1453-65.

47. Zhou H, Sun L, Yang XL, Schimmel P. ATP-directed capture of bioactive herbal-based medicine on human tRNA synthetase. Nature.

2013;**494**:121-4.

48. Pines M, Snyder D, Yarkoni S, Nagler A. Halofuginone to treat fibrosis in chronic graft-versus-host disease and scleroderma. Biol Blood Marrow Transplant. 2003;**9**:417-25.

49. Pines M, Knopov V, Genina O, Lavelin I, Nagler A. Halofuginone, a specific inhibitor of collagen type I synthesis, prevents dimethylnitrosamine-induced liver cirrhosis. J Hepatol. 1997;**27**:391-8.

50. Gnainsky Y, Spira G, Paizi M, Bruck R, Nagler A, Abu-Amara SN, et al. Halofuginone, an inhibitor of collagen synthesis by rat stellate cells, stimulates insulin-like growth factor binding protein-1 synthesis by hepatocytes. J Hepatol. 2004;**40**:269-77.

51. Lee JY, Kim DG, Kim BG, Yang WS, Hong J, Kang T, et al. Promiscuous methionyl-tRNA synthetase mediates adaptive mistranslation to protect cells against oxidative stress. J Cell Sci. 2014;**127**:4234-45.

국문초록

인간 threonyl-tRNA synthetase의 혈관신생인자 및 뮤신 생합성 조절 기전에 관한 연구

정 승 재
약학과 의약생명과학전공
서울대학교 대학원

아미노아실-tRNA 합성효소 (aminoacyl-tRNA synthetase, ARS)는 아미노산을 tRNA에 결합시키는데 필요한 효소로서 단백질 합성에 필수적인 요소이다. 최근 연구에 따르면 일종의 '하우스키핑 (houskeeping)' 효소로 여겨지는 ARS가 전사, 번역, 증식, 염증, 혈관신생 및 세포사멸과 같은 다양한 기능에 참여하고 있다는 것이 밝혀졌다. 이번 연구에서는 인간 threonyl-tRNA synthetase (TRS)와 그 잠재적인 역할에 주목하였다. 1장에서는 인간 TRS가 eIF4E 상동성 단백질 (eIF4E homologous protein, 4EHP)과의 상호작용을 통해 척추동물 특이적 번역 개시를 조절하기 위한 번역 개시 인자로서 기능한다는 것을 발견하였다. TRS와 4EHP의 선택적 상호작용은 eIF4E와 eIF4G의 상호작용과 유사한 방식으로 이루어지고, TRS가 eIF4A를 포함하기 위한 발판 단백질로서 작용함으로써, 결과적으로 eIF4F 유사 복합체를 형성하게 된다. 또한, 내피 세포 이동 과 혈관 형성, 지브라 피쉬 배아 혈관 형성 검사를 통해 이런 복합체의 형성이 척추동물 계통의 발달에 필요한 mRNA의 부분 집합 단백질 합성을 제어하는 진화적 기능을 포함한다는 것을 입증하였다. 2장에서는 TRS의 효소 활성을 통한 암세포에서의 새로운 기능에 관한 연구결과를 보고하였다. 먼저, 인간 췌장암 세포에서 과 발현된 MUC1

단백질의 양이 트레오닌에 의해 영향 받는다는 것을 발견하였고, MUC1의 단백질 양이 단백질 합성을 위한 트레오닌을 tRNA에 옮기는데 필수 효소인 TRS에 의해 영향을 받는다는 것도 확인하였다. 또한 TRS가 MUC1 단백질 생합성을 통해 췌장암 세포의 이동에 영향을 미친다는 것을 증명하였고, 췌장암 세포에 TRS 억제제를 처리하면 MUC1의 단백질 양이 감소하고, 세포의 이동이 저해되는 것을 관찰하였다. 마지막으로 췌장암 환자의 조직에서 TRS와 MUC1의 과 발현이 상관관계가 있다는 것과 생물정보학적 분석법을 통해 TRS와 MUC1의 발현이 췌장암 환자의 전반적인 생존율과 관련이 있다는 것을 보여주었다.

요약하자면, 1장의 연구에서 척추동물의 번역 개시 조절에 TRS가 예기치 않게 역할을 한다는 것을 보고하였고, 이는 척추동물에서 기능의 진화적 이득을 나타내는, 기존에 확인되지 않은 cap- 의존성 번역 개시 매커니즘을 발견한 것이라고 할 수 있다. 2장의 연구에서는 MUC1의 생합성을 강화하여 인간 췌장암 세포의 이동에 영향을 주는 TRS의 잠재적인 역할에 대한 몇 가지 증거를 제공하였고, TRS 억제제가 MUC1의 양과 암세포 이동에 미치는 영향을 보여줌으로써 TRS가 췌장암에 대한 새로운 표적이 될 수 있음을 제시한다고 할 수 있다.

주요어 : TRS, 4EHP, 구조결정, 번역 개시, MUC1, 췌장암, 세포이동

학 번 : 2008-21809